Influencing Optical and Charge Transport Properties by Controlling the Molecular Interactions of Merocyanine Thin Films

*Lukas Böhner[1], Philipp Weitkamp[1], Thorsten Limböck[1], Nora Gildemeister[1], Daniele Fazzi[1,2], Manuela Schie[3], Ruth Bruker[1], Dirk Hertel[1], Roland Schäfer[1], Klas Lindfors[1], and Klaus Meerholz[1]**

[1]Department of Chemistry, University of Cologne
Greinstraße 4-6, 50939 Cologne, Germany

[2] Universita di Bologna, Dipartimento di Chimica "Giacomo Ciamician",
Via P. Gobetti 85, 40129 Bologna, Italy

[3] Center for Surface and Nano-Analytics (ZONA)
Johannes Kepler University, Altenberger Str. 69,
Linz 4040, Austria

* klaus.meerholz@uni-koeln.de

Contents

Experimental Techniques and Methods

Sample Fabrication

Solution and Dispersion

The merocyanine HB238 was synthesized following ref. S1. It was dissolved in acetone (*Fisher Chemicals*, HPLC grade) with a concentration of $c = 1 \cdot 10^{-5}$ mol/l resulting in HB238 being present in the monomeric form in solution (see Figure S1). Aggregates in dispersion were prepared by transferring 0.1 ml of this solution into 0.9 ml of deionized water. We observed an instantaneous color change from deep blue to light purple.

The sample of dispersed aggregates for 2θ XRD scans (Figure S3a) was produced in the same way by using an HB238/acetone solution with a concentration of $c = 1 \cdot 10^{-2}$ mol/l. In this way HB238 aggregates of purple color precipitate visibly by eye. The precipitate was placed on a float glass substrate with a pipette and allowed to dry overnight.

Spin-coated films on silicon dioxide surfaces

All spin-coated samples in this work were fabricated from HB238 in chloroform (*Fisher Chemicals*, HPLC grade) solutions with a concentration of $c = 1 \cdot 10^{-2}$ mol/l. Spin coating was then performed by dropping 0.1 ml of this solution onto the substrates (float glass*, Paul Marienfeld GmbH & Co. KG*) for transmission spectroscopy and luminescence excitation, ellipsometry (quartz glass, *Nano Quarz Wafer GmbH*), and transistor-measurements and PL-spectroscopy (OFET-substrates, *Fraunhofer IPMS, Dresden*). Subsequently the spin coater was started (static dispense). All samples were spun at 3000 rpm speed with 3000 rpm/s acceleration, and for 60 seconds. With these parameters film thicknesses of approximately 20 nm were obtained as determined using atomic force microscopy (AFM). Subsequent annealing was performed by placing the substrates on a preheated hot plate for 10 minutes directly after the spin coating process. The used temperatures are given in the main text. The OFET substrates were ozonized for ten minutes before use to enhance the surface polarity and thus to improve HB238 film formation. For every annealing temperature a separate sample was prepared.

Evaporated thin films on HOPG and float glass

The HOPG substrates were cleaved with scotch tape right before use in nitrogen atmosphere. Evaporation of HB238 was performed in a custom-built *CreaPhys GmbH* vacuum system with a

constant evaporation rate of 0.03 Å/s at a pressure of $2 \cdot 10^{-7}$ mbar onto HOPG substrates heated to 80 °C. For the mono- and multilayer samples, a nominal film thickness of 2.5 nm and 20 nm was evaporated, respectively. For the evaporation on float glass a nominal film thickness of 20 nm was deposited under the same conditions described above, using the same float glass substrates as in the spin coating study.

Optical Spectroscopy

Transmission and reflection spectroscopy were performed with a *PerkinElmer Lambda 1050* Spectrophotometer equipped with a removable linear polarizer and a rotatable sample mount, using a transmission 3-detector module or a universal reflectance accessory module. Both transmission and reflection spectroscopy were performed with macroscopic beam sizes of approximately 10 mm^2 area. All absorption spectra shown in this work were corrected by dividing the measured intensities of the fabricated samples by the blank substrate/cuvette spectra under the same experimental conditions (i.e. angle of incidence and polarization or pure solvent).

H- and J-transition peaks are known to be asymmetric. This is because H- (J-) transitions are energetically located at the exciton band-top (-bottom), thus only mixing with energetically lower (higher) lying states, which broadens the observed spectral peaks asymmetrically.[S2] Thus, absorption peak parameters were determined by fitting the data using asymmetric pseudo-Voigt profiles, having different widths on the high and low energy wing of the peak. The absolute peak-width is then calculated as the mean of both widths. The data to be fitted was chosen such that for the J-transition, the absorption up to the photon energy corresponding to the half of the peak maximum at the high energy side of the peak was considered. Similarly, for the H-transition, the absorption from the photon energy corresponding to the half of the peak maximum at the low energy side of the peak was considered. This minimizes the influence of spectrally overlapping transitions (see SI for exceptions).

The PL microspectroscopy analysis was performed with an in-house built confocal microscopy setup, equipped with a 100x magnification, 0.8 NA objective (*Olympus*). The sample is positioned and scanned using a three-dimensional nanopositioning stage. The collected photoluminescence light is detected using a single-photon counting detector (*MPD*) for PL-imaging or a spectrometer (*Princeton Instruments, IsoPlane SCT 320*) for PL-spectroscopy. The excitation source is a tunable white light source (*NKT Photonics, SuperK EXTREME*) equipped with a spectral filter system

(*NKT Photonics, SuperK VARIA*). The excitation light is focused onto the sample using the microscope objective. The PL spectra were recorded with an excitation wavelength of 490 nm (the emission was filtered using a 635 nm long pass filter) and 555 nm (568 nm long pass filter) for the aggregate and monomer spectra shown in Fehler! Verweisquelle konnte nicht gefunden werden.**a** and **b**, respectively. All thin film PL-spectra in this work were recorded with an excitation wavelength of 600 nm (635 nm long pass filter). All spectra on thin films were recorded utilizing an excitation power below 1.5 µW to minimize photo-bleaching. Fitting of J-transition emission peaks was performed applying the same procedure as for absorption peaks mentioned before, where here the fitting boundaries were chosen at the energy value which corresponds to half the peak maximum at the low energy side.

The luminescence excitation analysis (Figure S2) was executed using the same PL-setup. Spectra were collected on the same sample position for different excitation wavelengths (460 nm – 730 nm, in 10 nm steps), and a 750 nm long pass emission filter was used in the emission path. To determine the total emitted signal for each excitation wavelength, the emission spectra were fitted using a Lorentz peak function for the J-transition emission peak. The total emitted power was corrected with the power of the excitation beam. The excitation power was kept below 0.15 µW for all spectra, to minimize photo-bleaching. At the end of the experiment the photo-bleaching was approximately 25 %. Photo-bleaching can thus not be neglected but the general shape of the luminescence excitation spectrum is revealed.

The complex refractive index of the films was determined using variable angle spectroscopic ellipsometry using an M-2000-XI (J.A. Woollam) and analyzed using the CompleteEASE software (version 6). Standard spectroscopic ellipsometry in reflection (SEr), normal incidence transmission intensity as well as variable angle transmission spectroscopic ellipsometry (SEt) scans have been simultaneously fitted using the multi-sample analysis option. The angles of incidence for SEr were from 45° to 75° in steps of 5°, and from 0° to 65° in steps of 5° for SEt. The spectral range was from 245 nm 1690 nm. The transparent regime from 900 nm to 1690 nm was used to determine the sample layer thickness by a Cauchy model fit also accounting for incoherent backside reflections. Conversion to uniaxial anisotropic B-spline and wavelength expansion fit was performed subsequently with fixed layer thickness. Node spacing was set to 0.1 eV (0.2 eV) for the in-plane (out-of-plane) components and further lowered in the absorbing spectral regions. An

MSE of 6.2 was obtained for the multi-sample analysis. The model-free B-spline fit gives a very good match of the transmission intensity data.

Atomic Force Microscopy (AFM)

All measurements were performed with an *Asylum* research AFM (*Oxford Instruments*, *MFP−3D Infinity*) in alternating contact mode utilizing AC200TS cantilevers (*Olympus*). Data evaluation was performed using the software *Gwyddion*. Due to the undulating nature of the HOPG surface, the associated data images were processed by subtracting a polynomial background to improve the visual contrast resulting in the images shown in Fehler! Verweisquelle konnte nicht gefunden werden.**a** and **c**. The evaluation of height profiles was performed before background subtraction.

Electrical characterization

Transistor measurements were performed using a *Keithley, 4200A-SCS Parameter Analyzer*. The OFET-substrates have 16 drain-source electrode pairs. The substrate is highly doped silicon with a 300nm thick gate oxide. The devices have channel-lengths from 2.5 µm to 20 µm and a channel−width of 1 cm. In this study, for every sample at least three devices with a channel-length of 20 µm were used for evaluation. The charge carrier mobility was determined from the transfer characteristics using the formulas[S3]

$$\mu_{linear} = \frac{\partial I_D}{\partial V_G}\frac{L}{WC_{SiO_2}V_D}, \text{ and} \qquad \textbf{(eq. 1)}$$

$$\mu_{saturation} = \left(\frac{\partial\sqrt{I_D}}{\partial V_G}\right)^2 \frac{2L}{WC_{SiO_2}}, \qquad \textbf{(eq. 2)}$$

where μ_{linear} and $\mu_{saturation}$ are the hole mobilities in the linear and saturation regime, respectively, I_D is the drain-current, V_G is the gate-voltage, L and W are the channel-length and –width, C_{SiO_2} is the gate-dielectric capacitance per unit area, and V_D is the drain-voltage. The derivatives in **eqs. 1** and **2** were evaluated from a linear fit to the measured dependence of the drain-current or the square root of the drain current on the gate-voltage in the linear regime (fitting range of gate voltage from −20 V to −50 V), or saturation regime (fitting range of gate voltage from −20 V to −40 V), respectively (see Figures S19 and S20). The corresponding transfer characteristics were recorded from +10 V to -50 V gate voltage at a constant drain voltage of -10 V or -130 V in the linear and saturation regime, respectively.

X-ray Diffraction (XRD)

The diffraction patterns were recorded with an *Empyrean* diffractometer (*Malvern Panalytical*) in 2θ geometry. The measurements were performed with a Cu K-α X-Ray source using a fixed divergence slit with a slit size of 0.0286. The structure of single crystals was determined using a *Bruker D8-Venture* with kappa-geometry equipped with a Cu *Microfocus* X-Ray source and a *PhotonIII M14* detector. The disordered solvent molecules included in the crystal were treated with the software *PLATON SQUEEZE*[S4], and single crystal structure determination and refinement were performed using the software *SHELXT*[S5] and *SHELXL*[S6], respectively.

Quantum chemical calculations

Density functional theory (DFT) calculations by using the range separated functional ωB97X-D and 6-311G** basis set were employed to obtain the equilibrium molecular structure and vibrational force field of HB238. Excited states, namely vertical transitions, were computed by TD-DFT calculations. The dipole active excited state S1 was optimized, and the vibrational force field was computed at the same level of theory. In such a way, the Franck-Condon (FC) factors were computed considering the ground and excited state equilibrium geometries and force fields. The computed vibronic absorption spectrum in gas-phase is reported in Figure S1 where the TDDFT energies have been shifted by a 0.575 eV in order to match the experimental data[S15]. DFT calculations were performed using Gaussian16 (B.01 version).[S7] 34

The dynamic polarizabilities, the absorption spectrum and the induced charge densities of HB238 single crystal were computed via pseudopotential plane-wave DFT calculations using the suite of codes QuantumESPRESSO[S8] 35 coupled with the turboTDDFT [S9] 36. The latter efficiently implements a Liouville−Lanczos approach to time-dependent density functional theory for the calculation of the absorption spectra in the frequency domain. For such a calculation, the PBE-generalized gradient exchange−correlation functional and ultrasoft pseudopotentials from the PS library were used. Single-particle wave functions (charge density) are expanded in plane waves up to an energy cutoff of 70 Ry (700 Ry). Only Γ point has been considered for Brillouin zone sampling in the reciprocal space. Dynamic polarizabilities were computed with respect to the Cartesian coordinates, rather than crystallographic ones. Therefore, the z-axis coincides with **a**, y-axis with **b**, while x-axis differs from **c**, the latter showing an angle with respect to the **ab** plane (monoclinic unit cell, see **Fehler! Verweisquelle konnte nicht gefunden werden.d**).

Supporting Information Part I: General Optical and Structural Properties of HB238 Molecule and its Aggregates

The measured (in acetone) and calculated (in gas phase) absorption spectra of HB238 are shown in ***Figure S1*** to confirm the presence of uncoupled HB238 molecules in acetone solution.

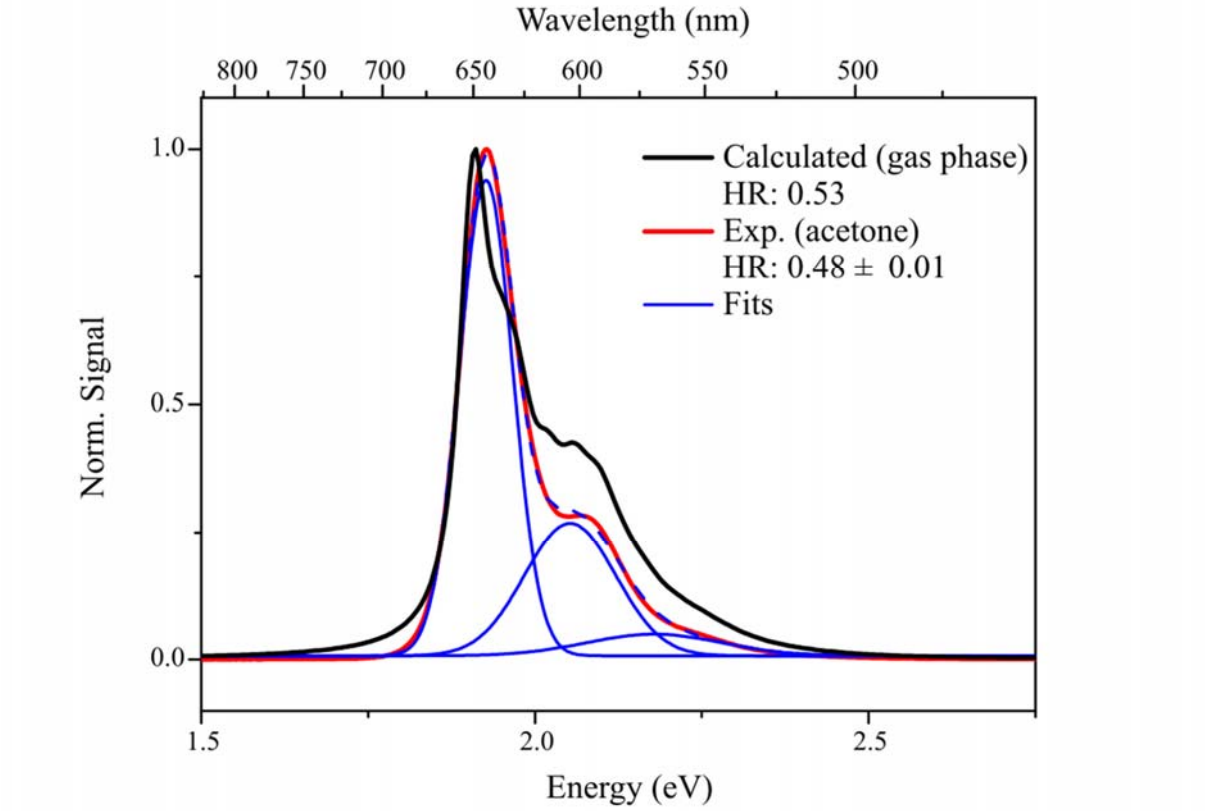

Figure S1*: Calculated (black, gas phase, TDDFT energies shifted by 0.575 eV to match the experimental data) and experimental (red, in acetone solution) HB238 monomer absorption spectra and effective Huang-Rhys parameters along with spectral fits to the experimental spectrum (blue).*

The spectral shape of the calculated and experimental absorption spectra agrees well. On top of that the calculated (HR: 0.53) and experimentally observed (HR: 0.48 ± 0.01) effective *Huang-Rhys* factors are similar. To obtain the *Huang-Rhys* factor from the experimental spectrum fitting was performed with the function[S10]

$$I_{abs}(E) = y0 + I_{total} \sum_0^n \frac{HR^n e^{-HR}}{n!\, w_n \sqrt{\pi/2}} \exp\left\{-2\frac{\left(E-(E_0+n\omega_{eff})\right)^2}{{w_n}^2}\right\}, \qquad \textbf{(eq. SI-1)}$$

where $y0$ is an offset, I_{total} is the integrated absorption spectrum, E_0 is the position of the zero-phonon line, and w_n is the width of the nth vibronic transition peak, and ω_{eff} is the effective phonon-energy. The *Huang-Rhys* factor is then obtained as fitting parameter.

Figure S2 shows the luminescence excitation spectrum along with the extinction spectrum of a spin coated thin film on float glass (AOI: 45°, p-polarized) annealed at 120 °C for 10 minutes. The excitation spectrum here is the PL-intensity of the J-transition as a function of the excitation photon energy. Small variations in the intensity of the excitation as a function of photon energy were corrected by normalizing the signals.

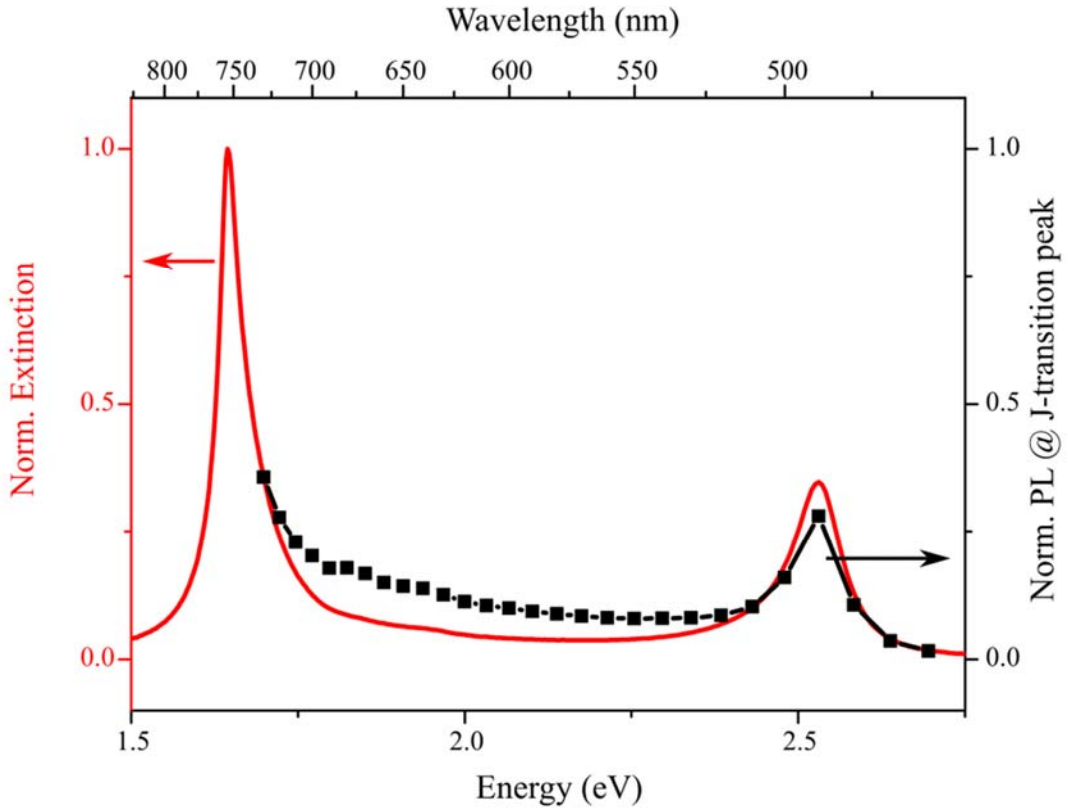

Figure S2*: Normalized luminescence excitation (black dots) and extinction (AOI: 45°, p-polarized, red solid line) spectra of a spin coated and annealed (120 °C) HB238 thin film on float glass. The spectra were normalized to match signals at 1.698 eV (730 nm) excitation.*

The excitation spectrum agrees well with the extinction spectrum and a local maximum is observed at the H-transition energy, elucidating that J-transition emission is observed upon excitation of the H-transition. This proves the coupled nature of the two transitions. Excitation was performed using a 0.8 NA microscope objective. Light is thus incident on the sample within a cone up to an angle of incidence of approximately 50°.

X-Ray diffraction patterns of the different samples investigated in this work were obtained by 2θ-XRD measurements, shown in ***Figure S3*a** along with the simulated powder pattern of the single crystals obtained from mesitylene solution (CCDC: 2073461).[S11] The measured samples exhibit only one significant diffraction peak at approximately 2θ = 5° suggesting identical crystalline arrangement in all samples. The simulated powder pattern is dominated by a diffraction peak at around 2θ = 4.8°, close to the diffraction peak of the other samples. The measured single crystal contained solvent inclusions which may lead to slight distortions, possibly resulting in the observed peak shift. These solvent molecules have been excluded by using the software *PLATON SQUEEZE*[S12] resulting in the single crystal structure shown in ***Figure S3*b**. We assume that this single crystal structure represents the crystal structures present in the different samples investigated in this work.

The dominating diffraction peak around 2θ = 4.8° in the simulated pattern corresponds to the (2 0 0) crystallographic plane as shown in ***Figure S3*b**. If we assume the diffraction peak at approximately 2θ = 5° of the measured patterns to be associated with the same (or a synonym) (2 0 0) plane, then the absence of any other diffraction peak in the measured patterns suggests uniaxially anisotropy with upright standing molecules, as the (2 0 0) plane would then be (nearly) parallel to the surface. This agrees well with the uniaxial anisotropy found in optical experiments (main text **Figure 3**) and with the computational results (main text **Figure 4**), which reproduce the experimental absorption spectra, if the molecules are standing upright, relative to the substrate as shown in **Figure 4** in the main text. Only the sample of dispersed aggregates shows more peaks in its 2θ-XRD pattern. The additional peaks are however of low intensity. This can be explained by the fact, that these precipitated aggregates were placed on a float glass substrate with a pipette, which results in more isotropic arrangements. Besides the dominating diffraction peaks at approximately 2θ = 5°, the diffraction pattern of the dispersed aggregates has a comparable shape with the simulated powder pattern at higher angles. Additionally, for the determined monoclinic single crystal structure, the miller indices (2 0 0) correspond to a lattice plane distance of ≈ 1.9 nm, which agrees well with the observed HB238 thin film step-heights measured on HOPG (main text **Figure 7e**).

The observed fringes around the diffraction peaks of the thin film patterns originate from finite size effects of the approximately 20 nm thick films.[S13] The dispersed aggregates possess a larger thickness due to the aforementioned preparation method. Thus, in this case fringes originating from finites size effects are not observed. The diffraction pattern of the multilayer on HOPG shown in the bottom panel of ***Figure S3*a** exhibits an additional reflex at around 2θ = 13.5°, which however originates from the HOPG substrate. We could not observe any diffraction peak in the XRD pattern of the monolayer on HOPG, despite substrate reflexes, due to the low HB238-amount.

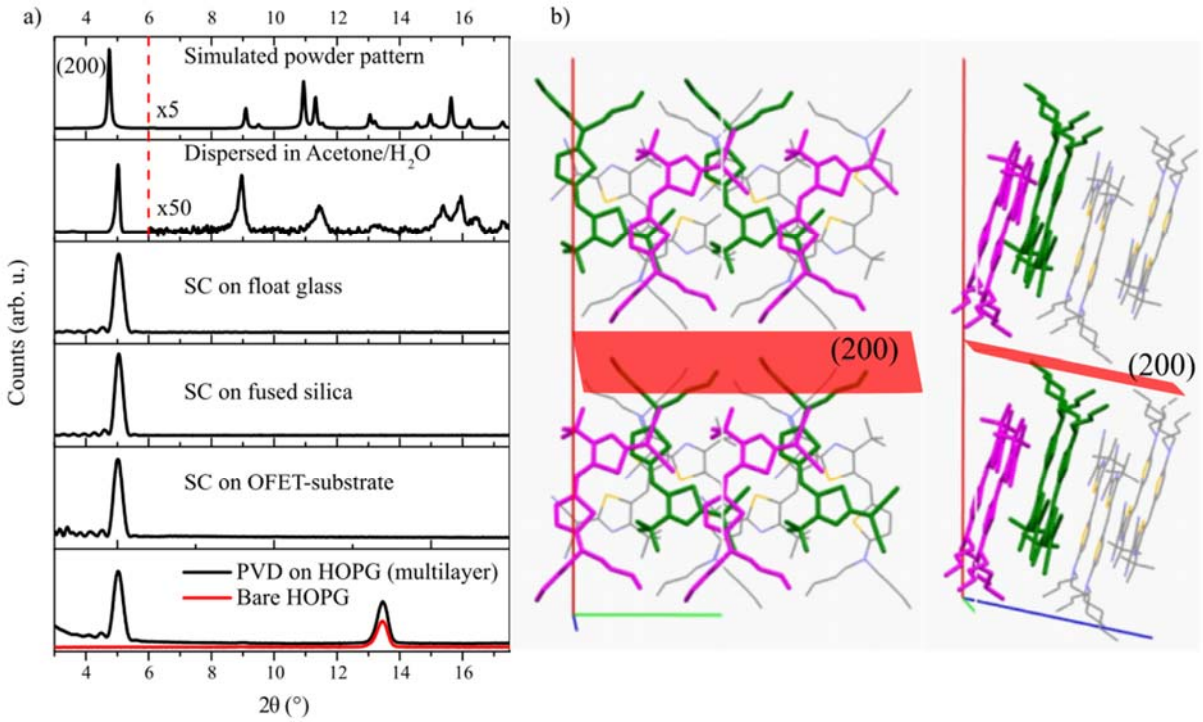

Figure S3*: a) 2θ-XRD scans of the different samples investigated in this work. From top to bottom: Simulated powder pattern of single crystal, dispersed in Acetone/water mixture, spin coated and annealed (120 °C, 10 min.) on float glass, fused silica, and OFET-substrate, and thermally evaporated on HOPG as multilayer. b) single crystal structure shown in two different projections, along with the (2 0 0) crystallographic plane.*

Supporting Information Part II: Charge Carrier Mobility in Context of Molecular Aggregation

An insight into the correlation of crystallographic, morphological, and optical properties of the spin coated thin films used for electrical and optical characterization is provided by XRD, AFM, optical absorption, reflection, and PL-microspectroscopy measurements. XRD measurements were performed for samples at all annealing temperatures used in this work. The characteristic diffraction peak at approximately $2\theta = 5°$ is observed as only reflex for all samples of **regimes II** and **III** and for higher annealing temperatures. No significant diffraction is observed for samples of **regime I**. The diffraction patterns are shown in ***Figure S4*** along with the integrated peak intensities as a function of annealing temperature. The three different regimes are clearly distinguishable as explained in the main text. AFM images (10 µm by 10 µm area) of HB238 thin films spin coated onto OFET-substrates and float-glass substrates are shown in ***Figure S5-Figure S9*** for all different annealing temperatures. For the respective annealing temperatures the morphologies on both substrates are remarkably similar, which is to be expected due to the similar chemical composition of both substrate surfaces. Additionally topographical distinctions can be made between the **regimes I** (a.f, 50 °C), **II** (80 °C – 110 °C), and **III** (120 °C – 160 °C), which are mentioned in the main text. The samples in **regime I** exhibit a structurally fine morphology and additionally crystalline-appearing features of elongated shape. In **regime II** the film surfaces do not exhibit the aformentioned elongated features. However, it still shows a structurally fine morphology. Starting from an annealing temperature of 120 °C in **regime III**, the thin films exhibit a more crystalline morphology with several bigger, elevated crystallites embedded into a the film consisting of smaller crystallites. Here the observed structural features do not appear elongated as in **regime I**. Starting from an annealing temperature of 170 °C pronounced depletion zones are observed. For none of the samples any kind of in-plane preferential order is observed. Finally, at 200 °C annealing temperature melting of the thin films is observed, whereby mono- and few-layer islands remain on the surface.

For further investigation of structure-(optical)-property-relationships PL-microspectroscopy experiments have been carried out on all thin films spin coated on OFET-substrates. Laser-scanning PL micrographs (20 µm by 20 µm area) along with representative spectra measured at the indicated positions in the micrographs are shown in ***Figure S10-Figure S16***. Additionally, the associated extinction spectra (AOI: 45°, p–polarized) of the spin coated thin films on float glass are shown for comparison. The dark spots in the middle of some of the PL micrographs arise from photobleaching during focusing of the laser just before the measurement. Again, here by PL-spectroscopy a distinction between the **regimes I-III** can be drawn and the PL-spectra coincide well with the absorption spectra, as expected. In **regime I** the spectra are broad and of poorly defined shape, whereas starting from **regime II**, the J-transition peak is dominating the spectra. In **regime II** we observe a fairly broad low (high) energy tail in the emission (extinction) spectra, whose intensity decreases with increasing annealing temperature from 80 °C to 110 °C. Finally, starting in **regime III** from an annealing temperature of 120 °C the low (high) energy tail in the emission (extinction) spectra disappears almost completely and the spectra are governed by only the narrow J-transition peak. The aforementioned depletion zones starting from an annealing temperature of 170 °C are visible in the PL micrographs, too. Additionally, the absorption spectra

at 170 °C and higher annealing temperatures, exhibit broadening of the J-transition absorption peak due to a (only slightly pronounced) high-energy spectral shoulder (**Figure S15Figure S16a**). The origin of this spectral shoulder is unclear and was not further investigated. The observed mono- and few-layer islands at an annealing temperature of 200 °C display J-transition emission peaks with a fairly broad low-energy tail, comparable with the emission spectra of samples of **regime II**.

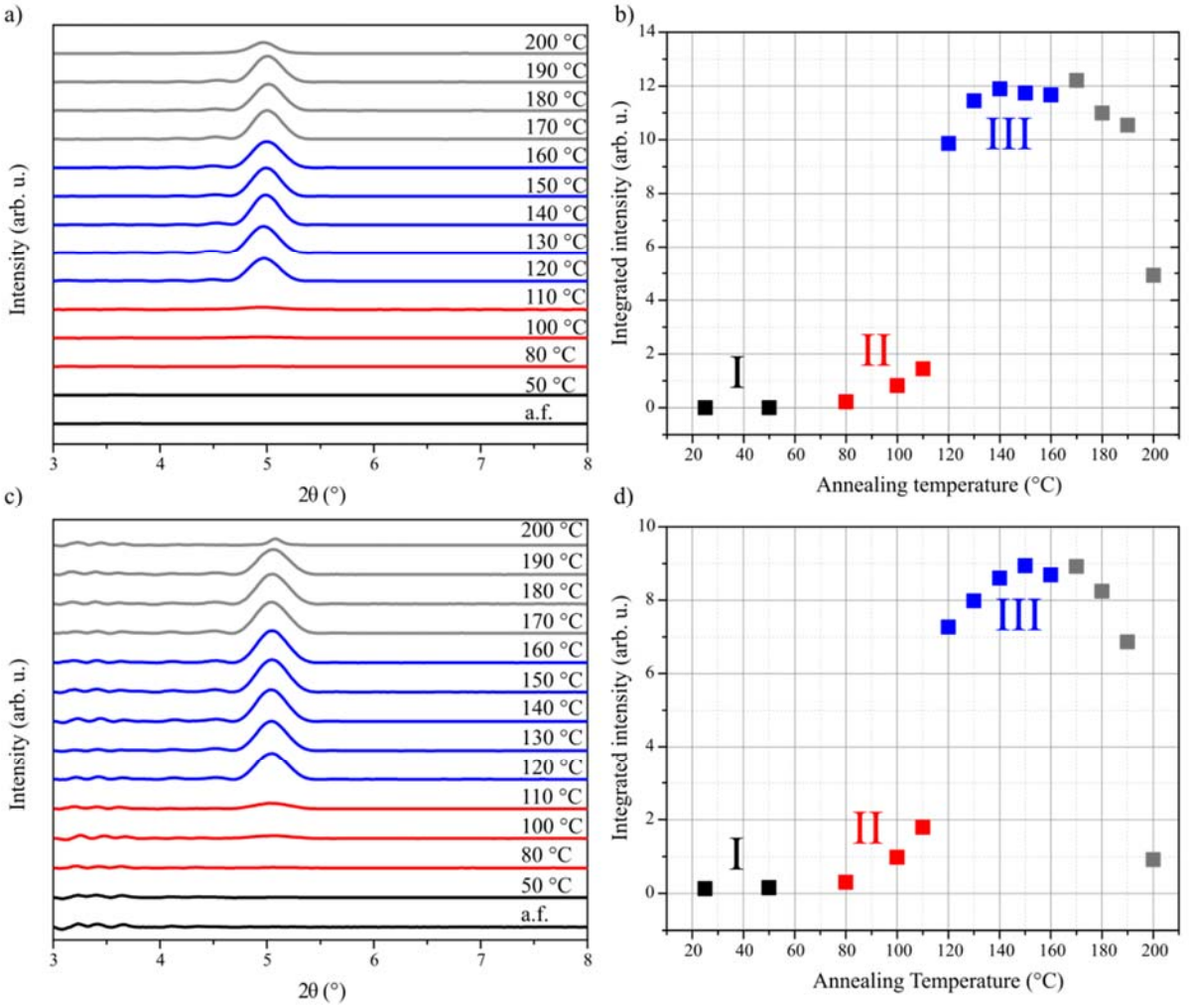

***Figure S4**: Comparative XRD investigations of spin coated HB238 thin films on float glass substrates and FET substrates. Diffraction patterns at different annealing temperatures and associated integrated peak intensities of the peak at $2\theta \approx 5°$ as a function of annealing temperature for thin films on glass substrates a) and b), and on FET substrates c) and d).*

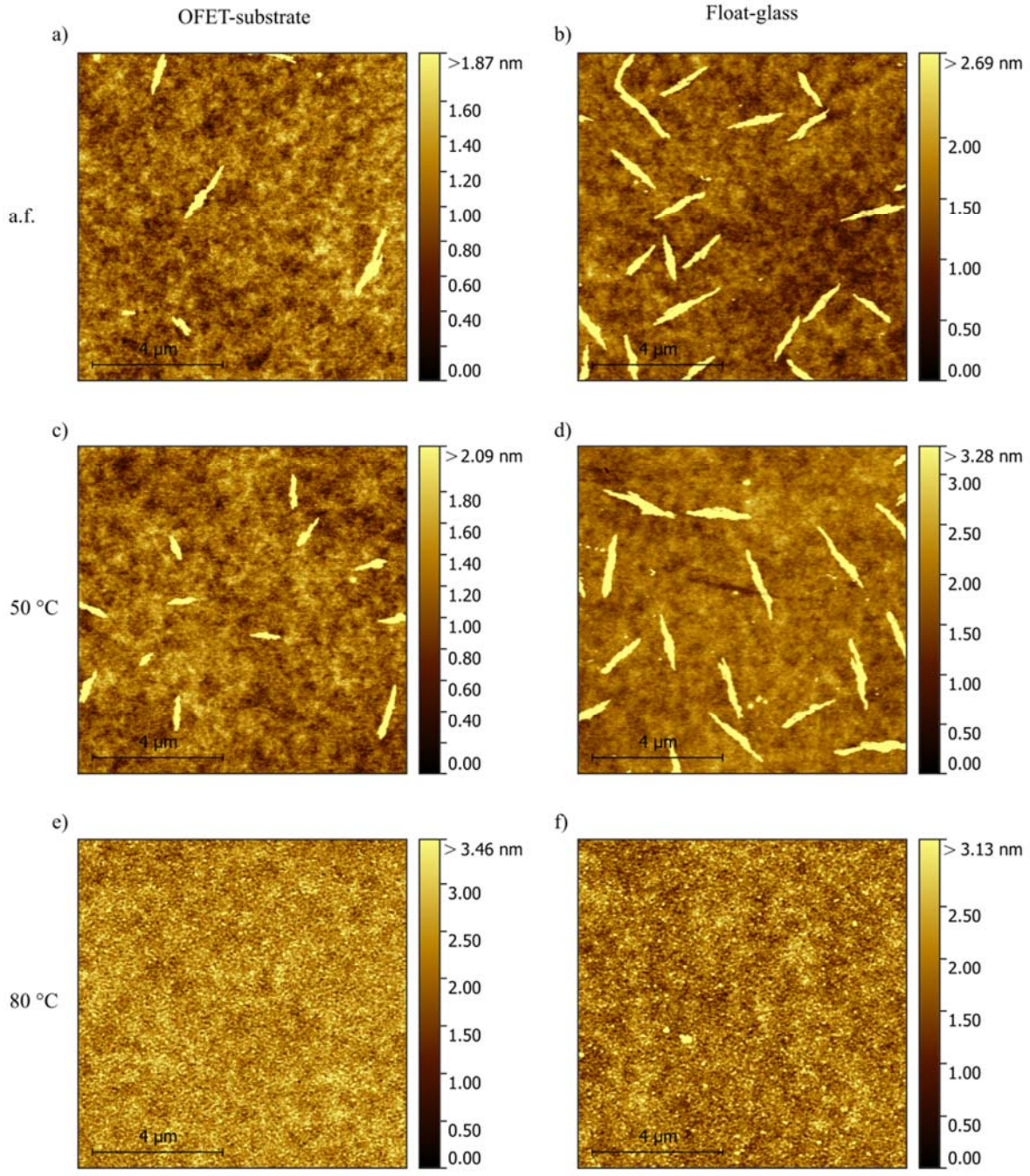

Figure S5*: AFM images (10 µm by 10 µm area) of HB238 spin coated on OFET (left; a, c, and e) and float glass substrates (right; b, d, and f), non-annealed (a.f.) and annealed at 50 °C and 80 °C, respectively. The corresponding annealing temperature is given on the left (****regime I – II****).*

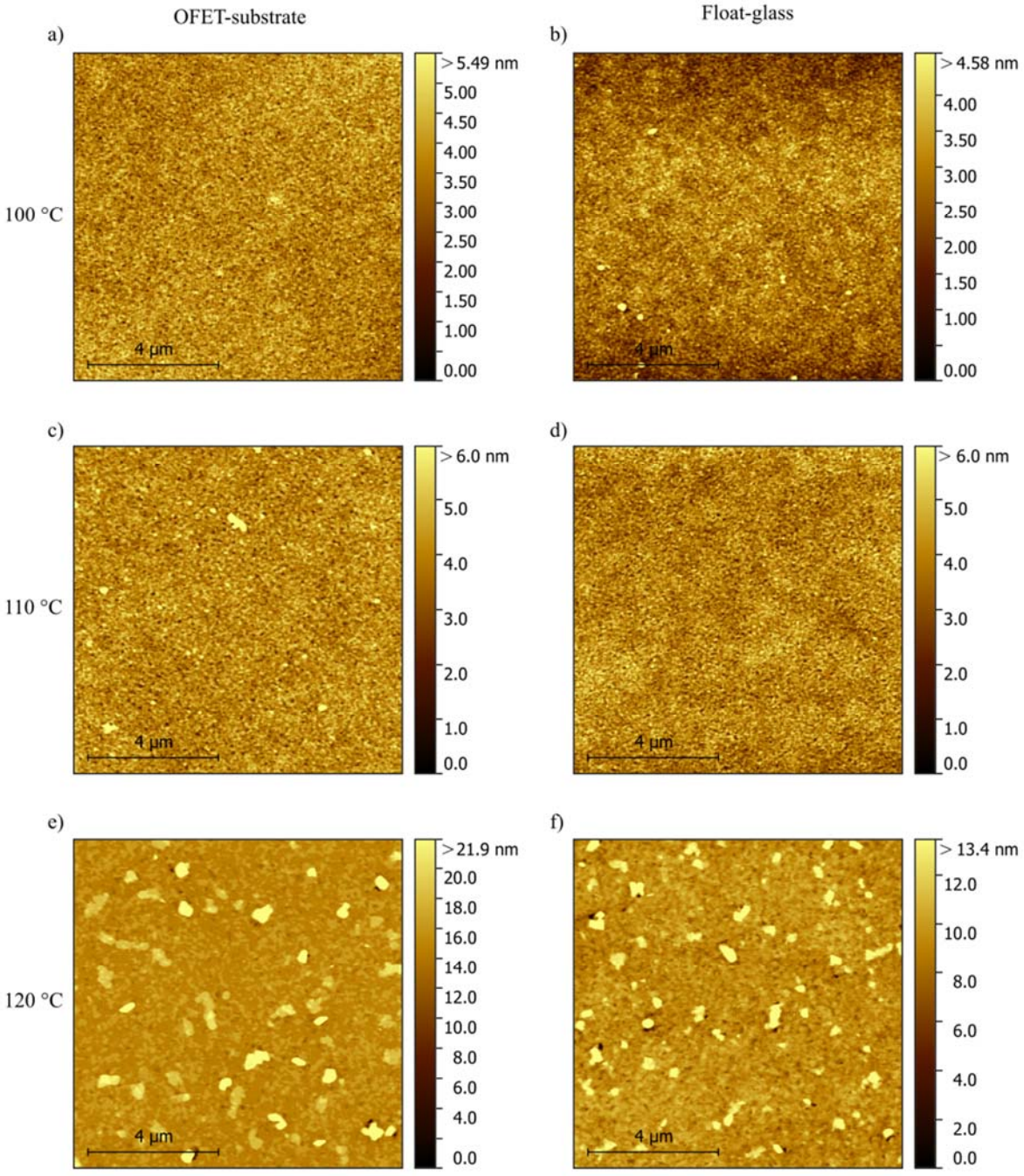

Figure S6*: AFM images (10 µm by 10 µm area) of HB238 spin coated on OFET (left; a, c, and e) and float glass substrates (right; b, d, and f), annealed at 100 °C, 110 °C and 120 °C, respectively. The corresponding annealing temperature is given on the left (****regime II – III****).*

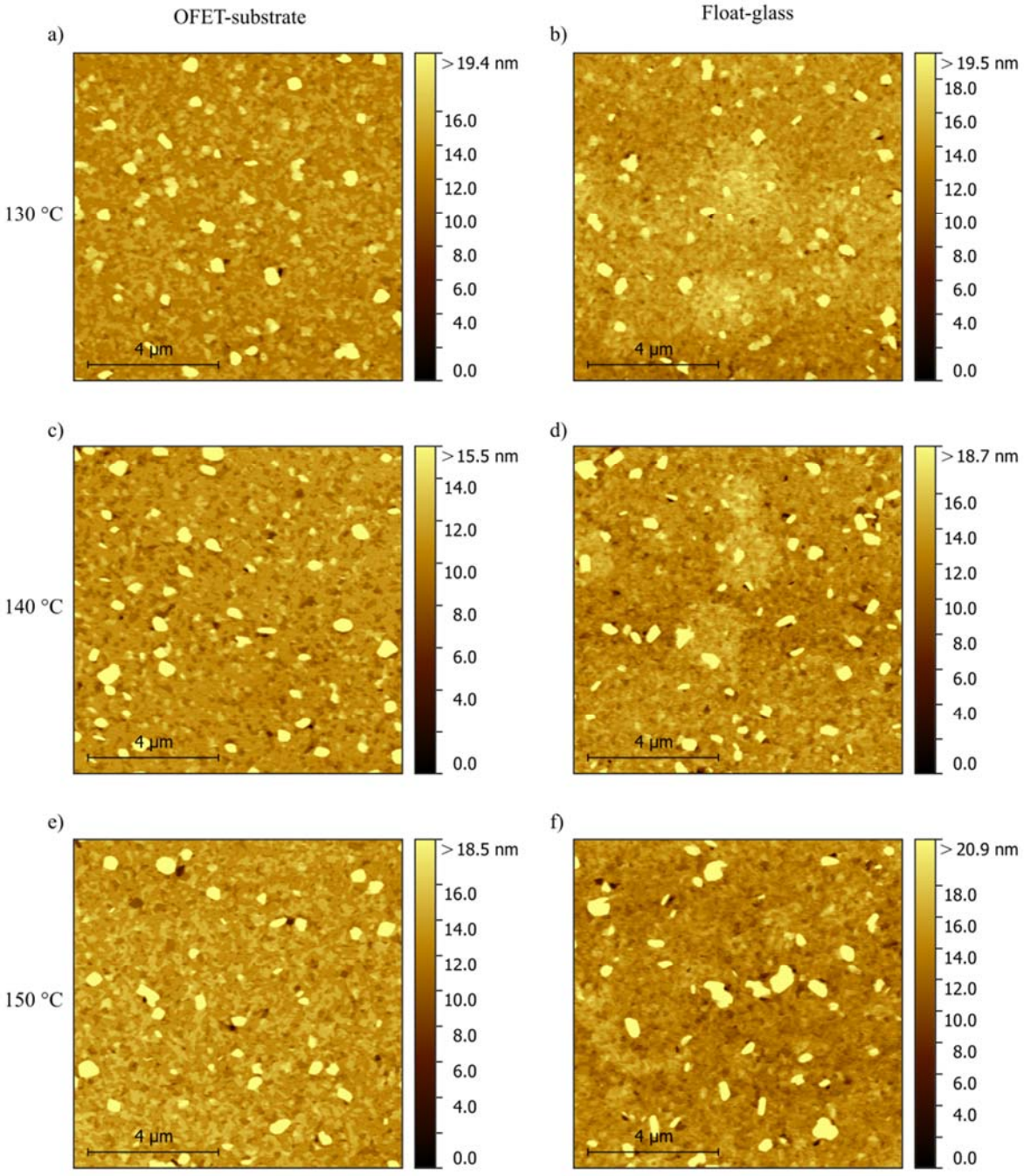

Figure S7*: AFM images (10 µm by 10 µm area) of HB238 spin coated on OFET (left; a, c, and e) and float glass substrates (right; b, d, and f), annealed at 130 °C, 140 °C and 150 °C, respectively. The corresponding annealing temperature is given on the left (****regime III****).*

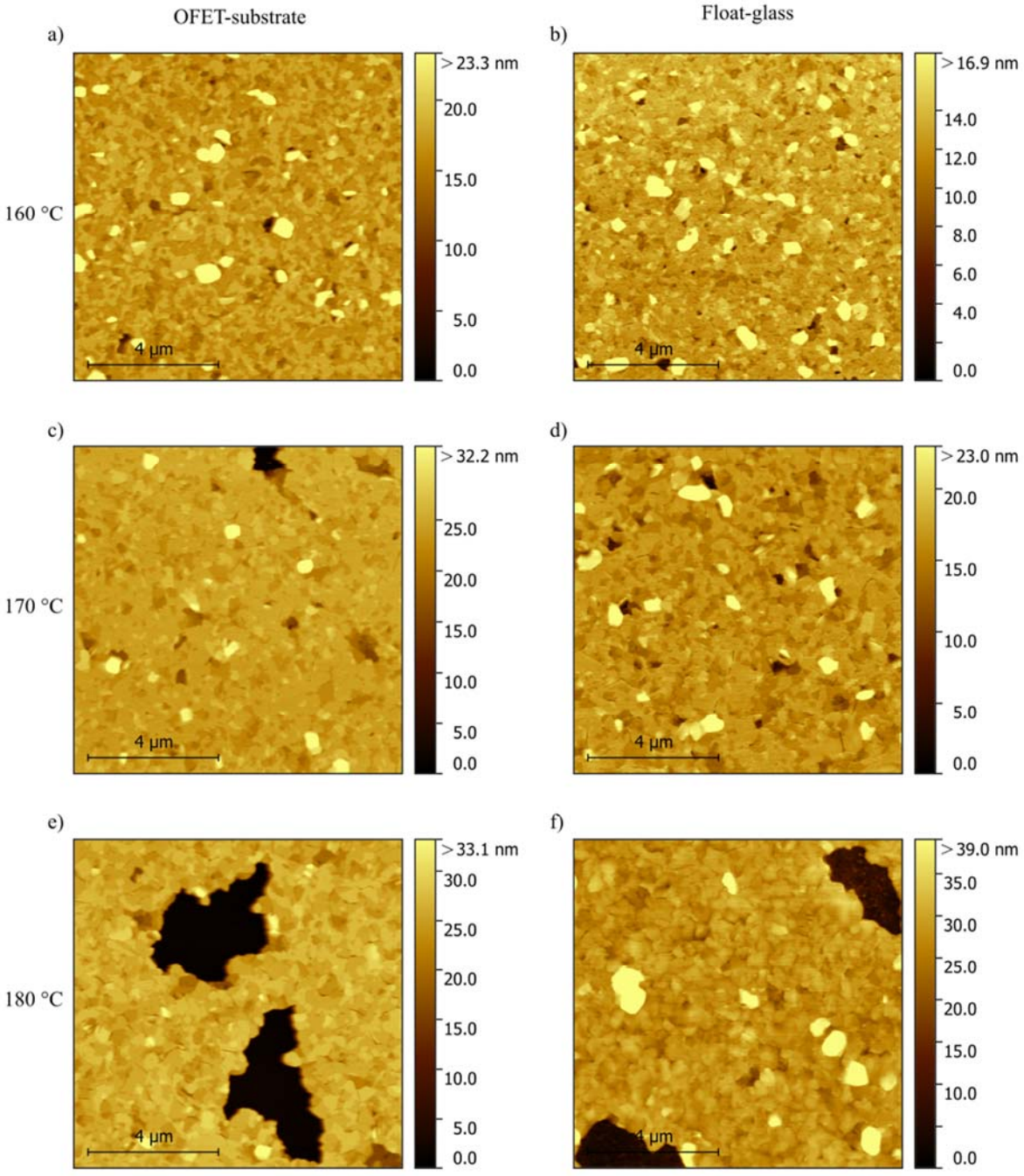

Figure S8*: AFM images (10 µm by 10 µm area) of HB238 spin coated on OFET (left; a, c, and e) and float glass substrates (right; b, d, and f), annealed at 160 °C, 170 °C and 180 °C, respectively. The corresponding annealing temperature is given on the left (****regime III*** *and beyond).*

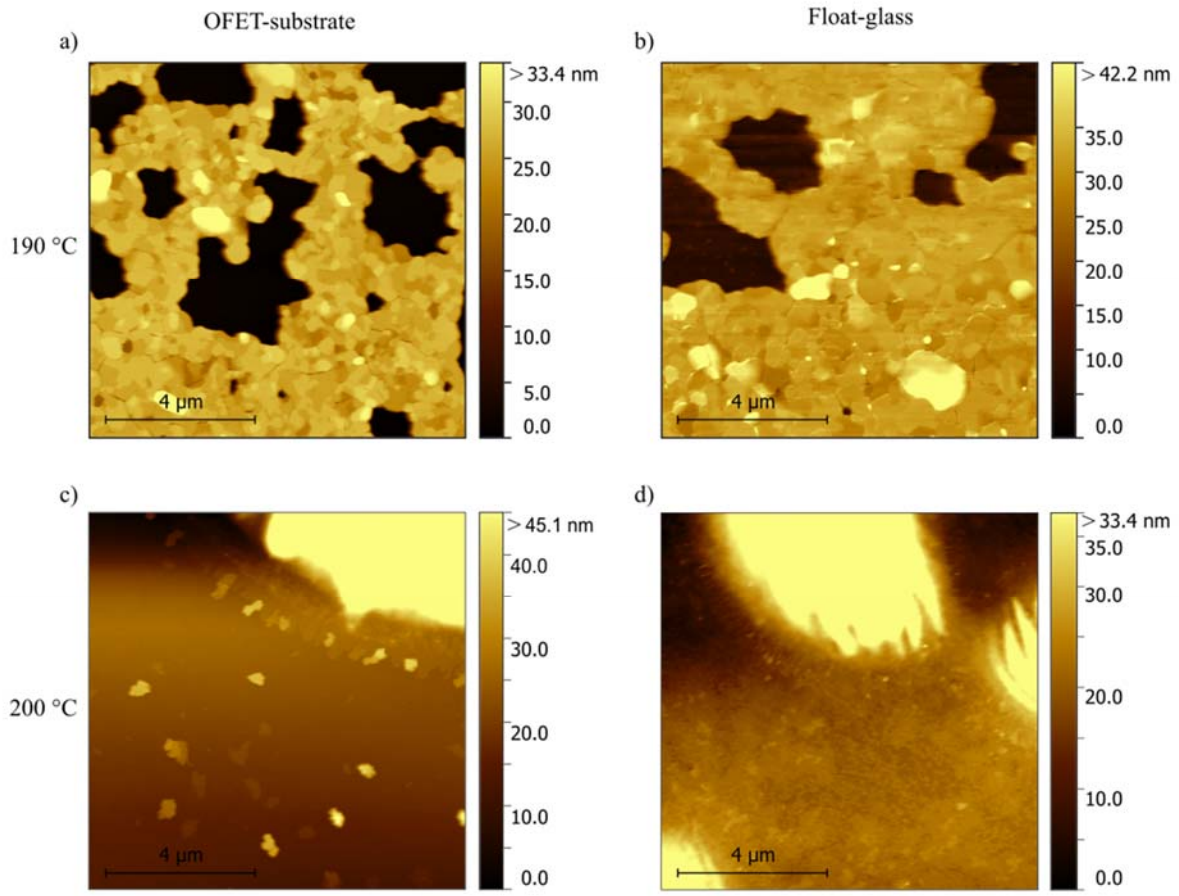

Figure S9*: AFM images (10 µm by 10 µm area) of HB238 spin coated on OFET (left; a and c) and float glass substrates (right; b and d), annealed at 190 °C and 200 °C, respectively. The corresponding annealing temperature is given on the left.*

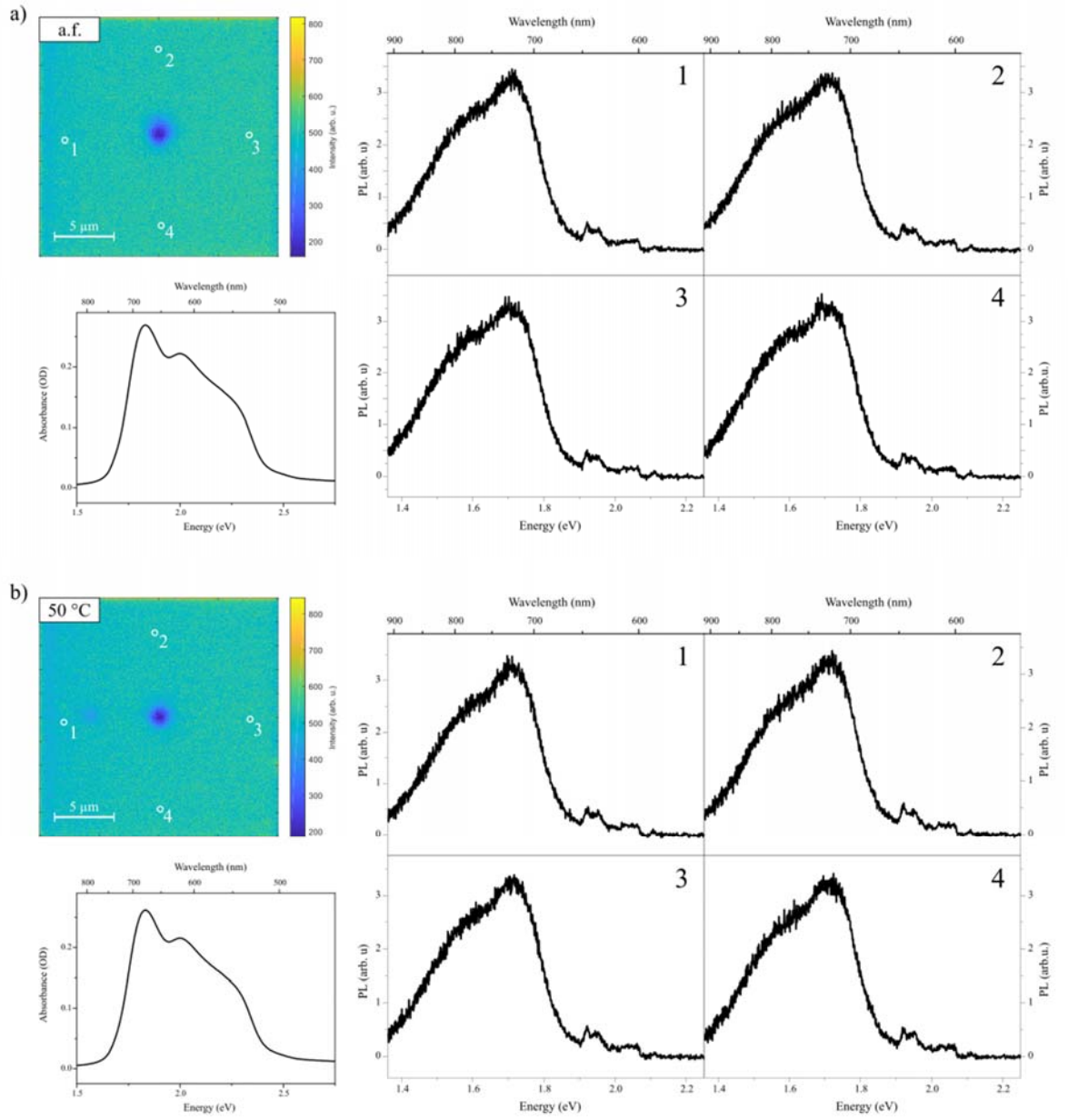

Figure S10*: PL micrographs (20 µm by 20 µm area, top left) on the OFET-substrates used for the extraction of charge carrier mobility in the main text (***Figure 5a****) along with representative PL-spectra (right) recorded at different positions indicated by white circles in the PL micrographs, and extinction spectra (bottom left) recorded on float-glass substrates fabricated by the same experimental procedure. The samples shown are the a) non-annealed (a.f.) sample and the sample annealed at b) 50 °C. Here, different from other samples, an excitation wavelength of 590 nm (600 nm LP filter) was used, as described in the main text.*

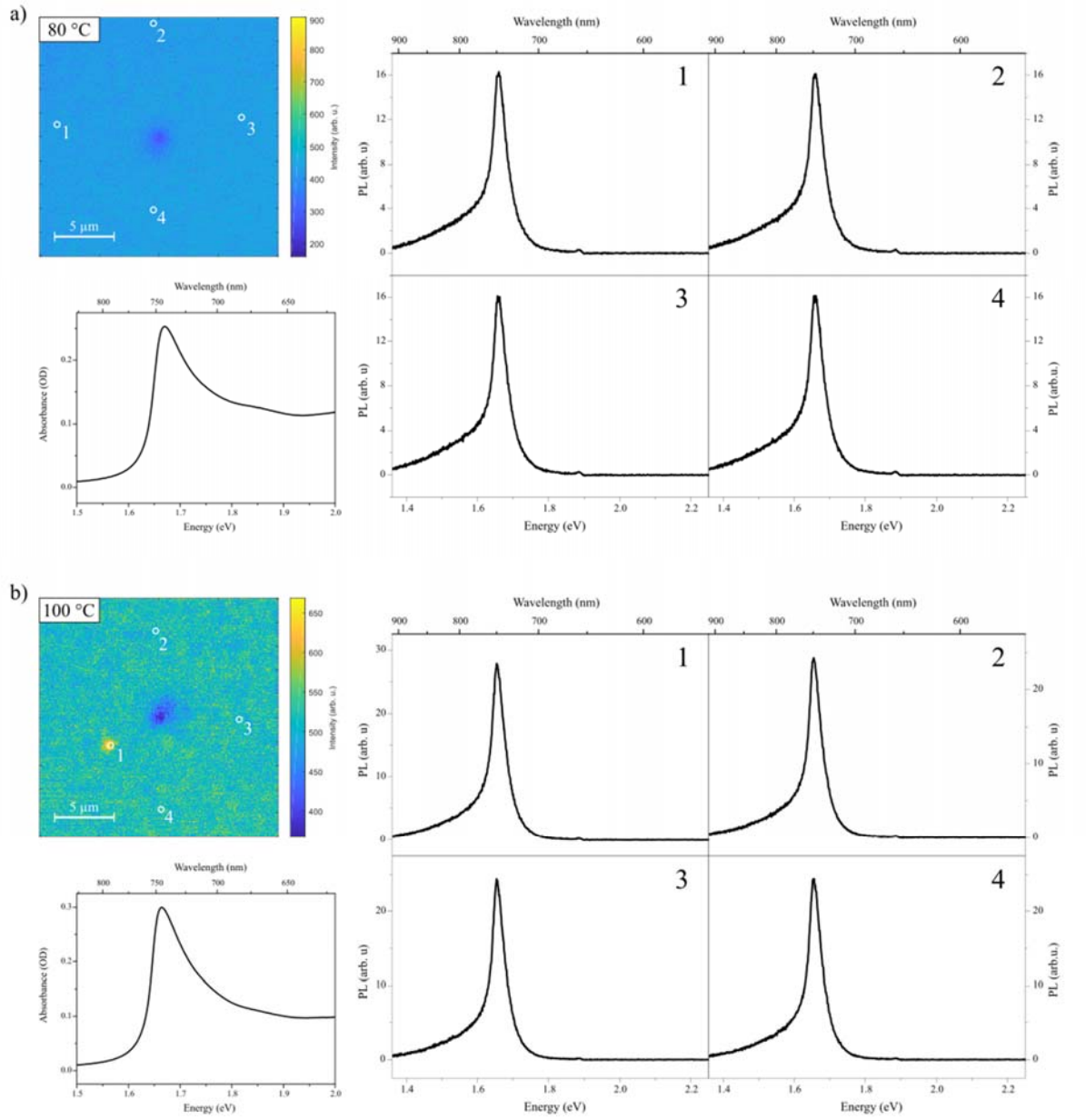

Figure S11*: PL micrographs (20 µm by 20 µm area, top left) on the OFET-substrates used for the extraction of charge carrier mobility in the main text (***Figure 5a****) along with representative PL-spectra (right) recorded at different positions indicated by white circles in the PL micrographs, and extinction spectra (bottom left) recorded on float-glass substrates fabricated by the same experimental procedure. The samples were annealed at a) 80 °C and b) 100 °C.*

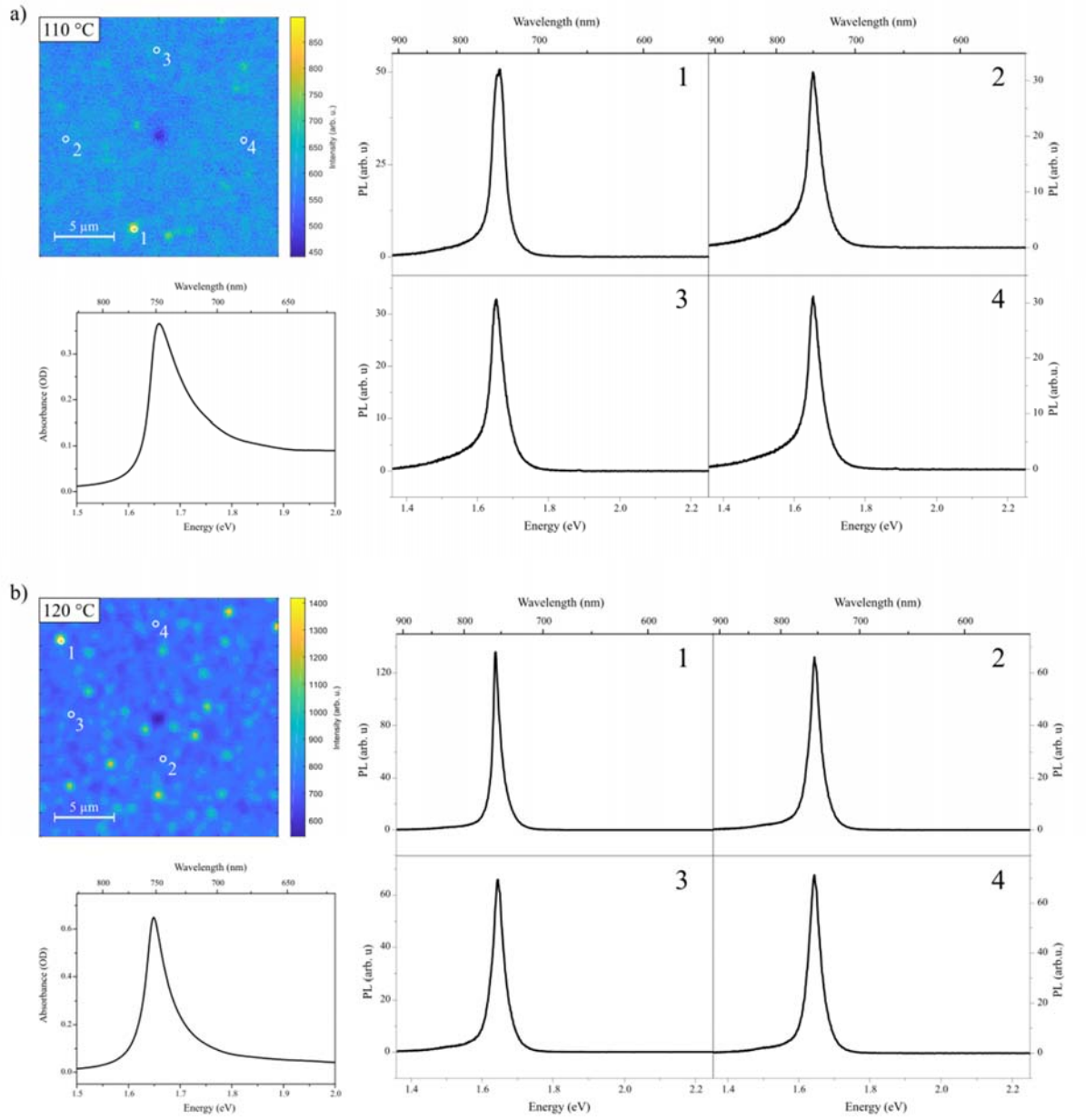

Figure S12*: PL micrographs (20 µm by 20 µm area, top left) on the OFET-substrates used for the extraction of charge carrier mobility in the main text (****Figure 5a****) along with representative PL-spectra (right) recorded at different positions indicated by white circles in the PL micrographs, and extinction spectra (bottom left) recorded on float-glass substrates fabricated by the same experimental procedure. The samples were annealed at a) 110 °C and b) 120 °C.*

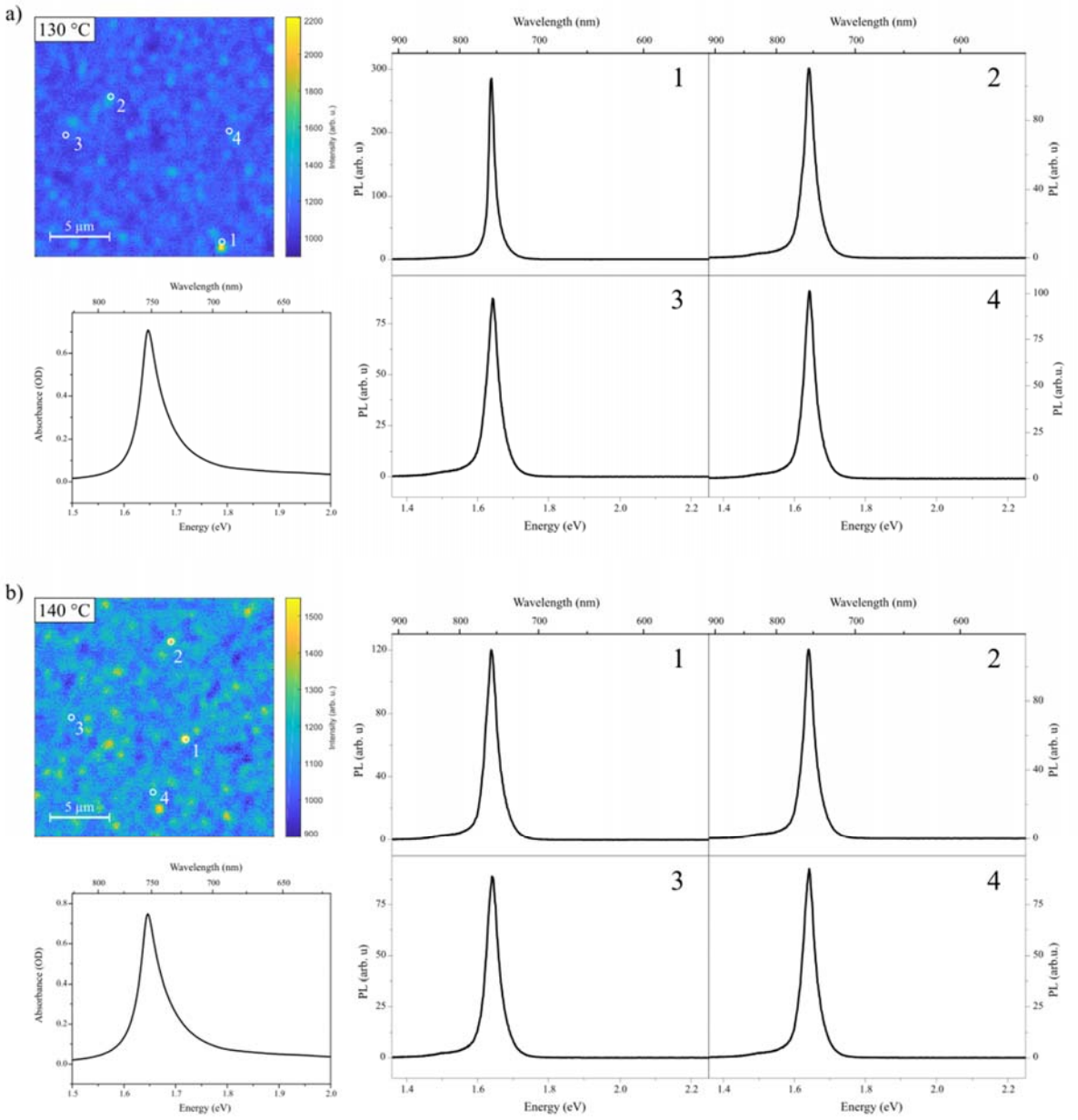

Figure S13*: PL micrographs (20 µm by 20 µm area, top left) on the OFET-substrates used for the extraction of charge carrier mobility in the main text (***Figure 5a****) along with representative PL-spectra (right) recorded at different positions indicated by white circles in the PL micrographs, and extinction spectra (bottom left) recorded on float-glass substrates fabricated by the same experimental procedure. The samples were annealed at a) 130 °C and b) 140 °C.*

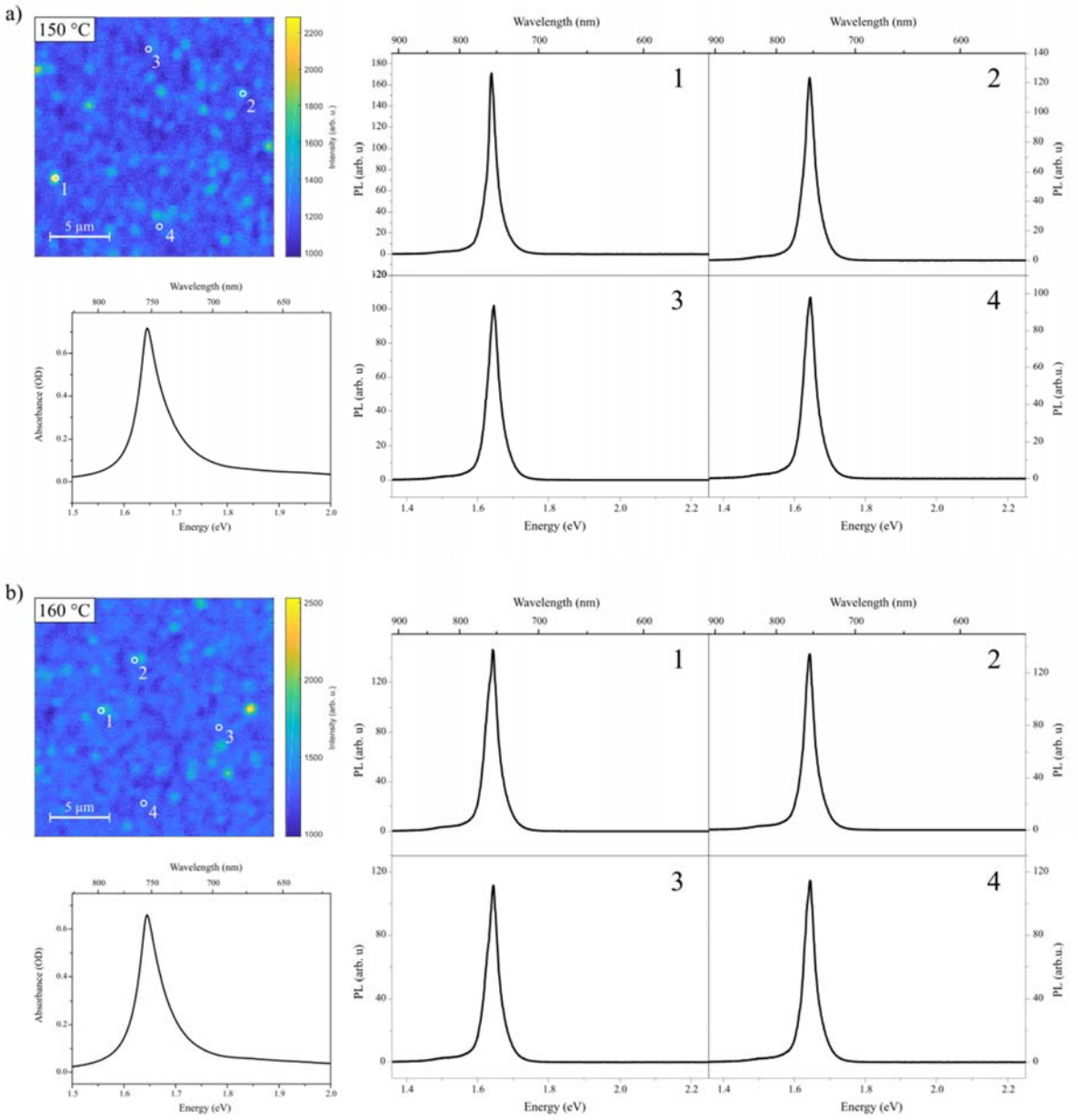

Figure S14*: PL micrographs (20 µm by 20 µm area, top left) on the OFET-substrates used for the extraction of charge carrier mobility in the main text (***Figure 5a****) along with representative PL-spectra (right) recorded at different positions indicated by white circles in the PL micrographs, and extinction spectra (bottom left) recorded on float-glass substrates fabricated by the same experimental procedure. The samples were annealed at a) 150 °C and b) 160 °C.*

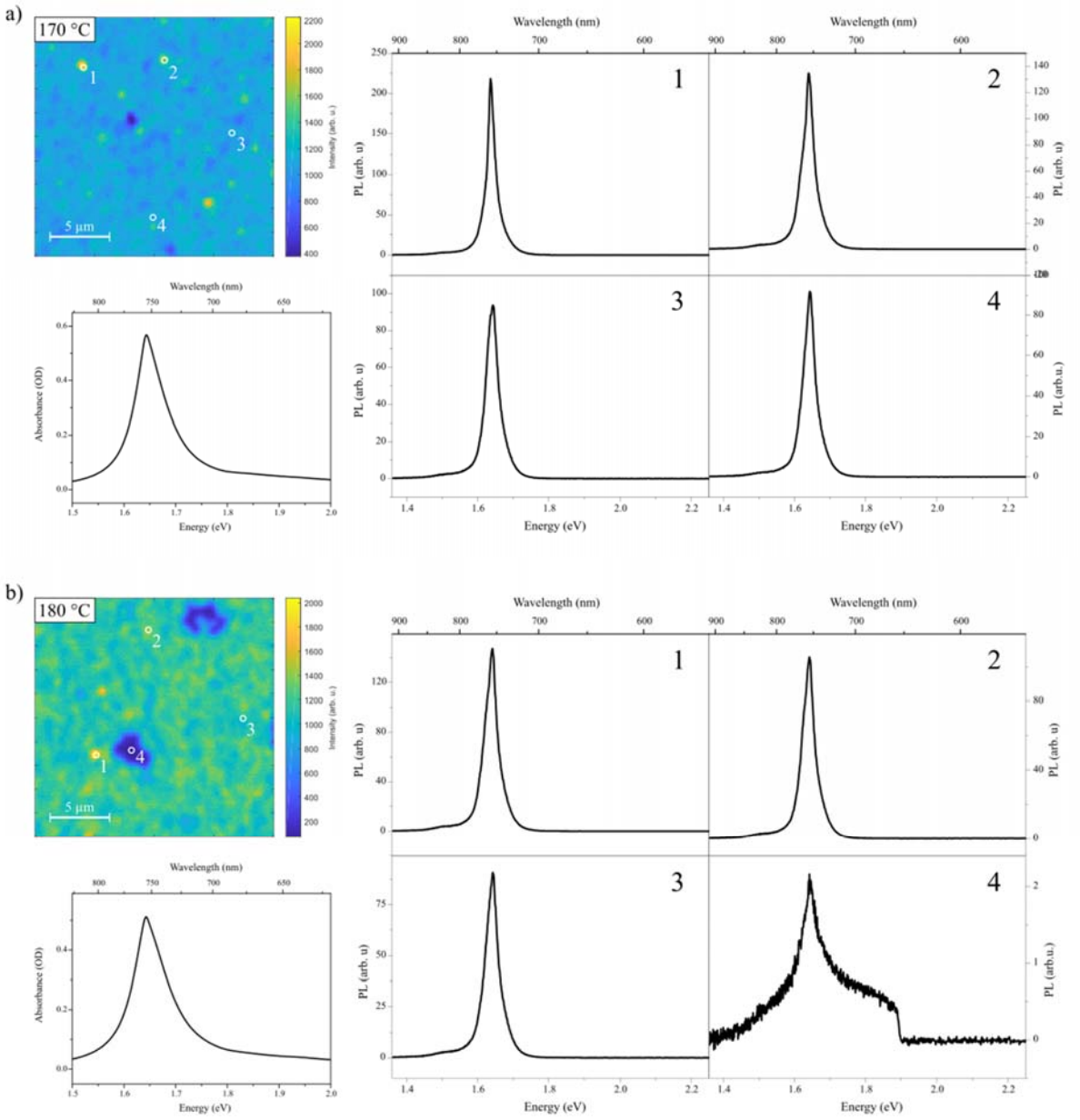

Figure S15*: PL micrographs (20 µm by 20 µm area, top left) on the OFET-substrates used for the extraction of charge carrier mobility in the main text (****Figure 5a****) along with representative PL-spectra (right) recorded at different positions indicated by white circles in the PL micrographs, and extinction spectra (bottom left) recorded on float-glass substrates fabricated by the same experimental procedure. The samples were annealed at a) 170 °C and b) 180 °C.*

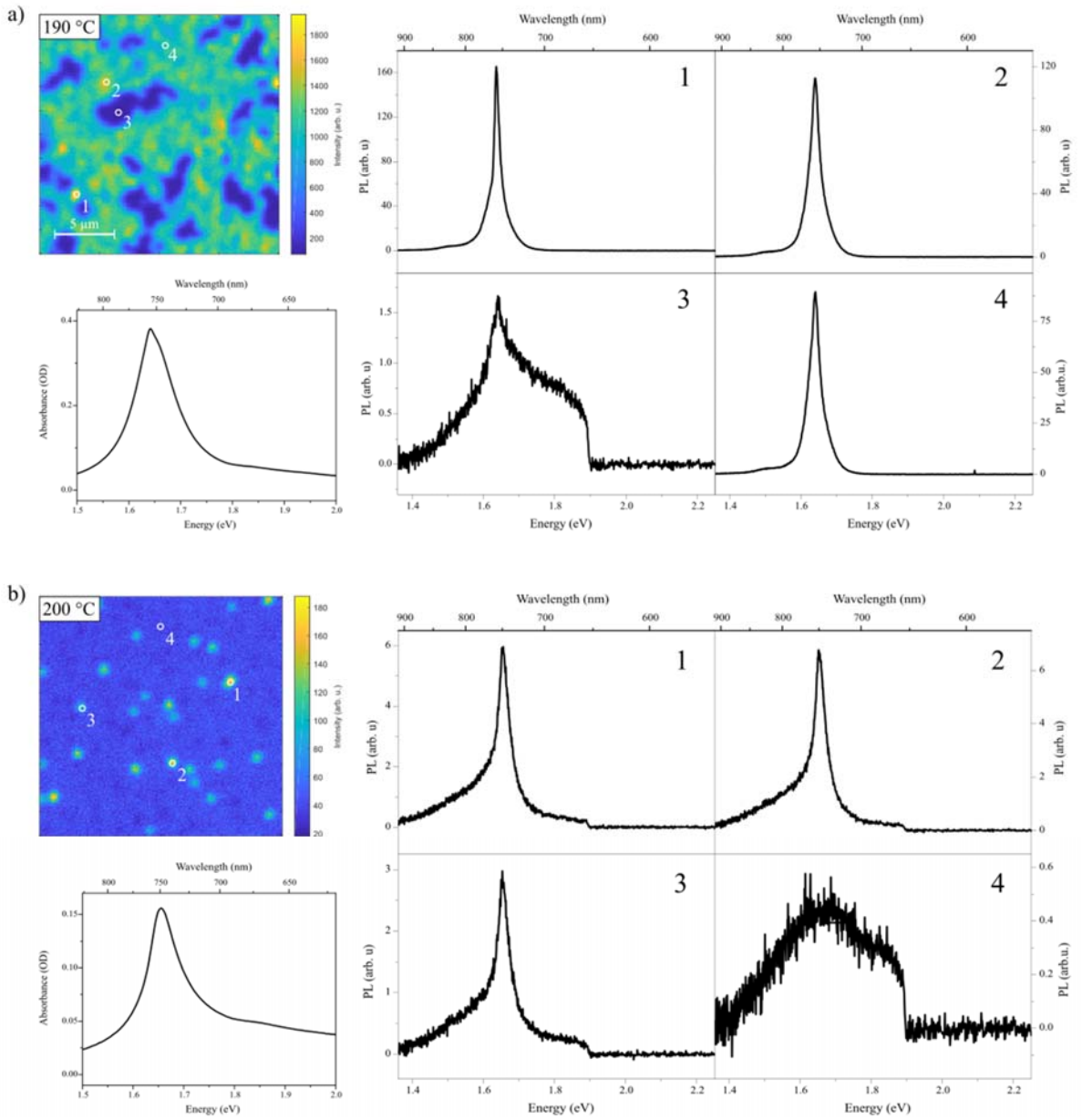

Figure S16*: PL micrographs (20 µm by 20 µm area, top left) on the OFET-substrates used for the extraction of charge carrier mobility in the main text (****Figure 5a****) along with representative PL-spectra (right) recorded at different positions indicated by white circles in the PL micrographs, and extinction spectra (bottom left) recorded on float-glass substrates fabricated by the same experimental procedure. The samples were annealed at a) 190 °C and b) 200 °C.*

Comparing the AFM and PL-microspectroscopy results with each other, a few further observations are made. The elongated structures observed in AFM height images of **regime I** (***Figure S5***) interestingly are not observed in PL micrographs (***Figure S10***). The emission images are completely homogeneous without any indication of the elongated structures and the recorded spectra exhibit identical spectral shape. Conclusively these elevated, elongated structures do not possess a different molecular packing from the surrounding film, or at least the molecular coupling in these structures is negligible, or absent, thus not resulting in any change of the emission.

The PL-microspectroscopy analysis of the samples in **regime III** reveals that the larger crystallites appear brighter in the PL micrographs. They thus emit stronger but show similar emission spectra as the surrounding thin film. We thus conclude, that all thin films in **regime III** entirely consist of the same kind of molecular aggregates. A few PL-spectra were collected within the comparably big depletion zones observed after annealing at 180 °C, or 190 °C (see spectrum **4** in ***Figure S15*****b** and spectrum **3** in ***Figure S16*****a**). These spectra still show the characteristic J-transition emission peak. However, they exhibit a fairly broad low energy tail as well as a broad spectral shoulder at higher energies. We assume, that due to the much lower amount of molecules in these depletion zones, aggregation can only take place incompletely and thus the spectra are comprised of aggregate-, monomer- and possible dimer- or oligomer-emission features.

Lastly, at an annealing temperature of 200 °C we observe isolated mono- and few-layer islands, which still show the characteristic J-transition emission peak. Its shape is similar to the emission spectra of samples in **regime II**. We thus assume a lower degree of aggregation compared with the aggreagted thin films of samples in **regime III**, due to the lower molecular density. In between the islands we observe a very broad and weak emission, similar to what is observed in the depletion zones of samples annealed at 180 °C and 190 °C. We can thus conclude, that the corresponding absorption spectrum, which displays the characteristic J-transition absorption peak is almost entirely caused by the observed mono- and few-layer structures.

Figure S17 shows the absorption spectra of thin films spin coated on float glass at all annealing temperatures discussed above at 45° AOI for p-polarized light and under normal incidence, to illustrate the anisotropic optical properties of the thin films. As discussed in the main text, the H-transition absorption peak is only visible if the incident light has an out-of-plane electric field component, due to the uniaxial anisotropic nature of the thin films. This is observed for all samples annealed at 120 °C or higher. Slight anisotropic behaviour is observed as well for lower annealing temperatures and even for the non-annealed sample. We thus assume the presence of low-molecular aggregates even if the sample is not annealed.

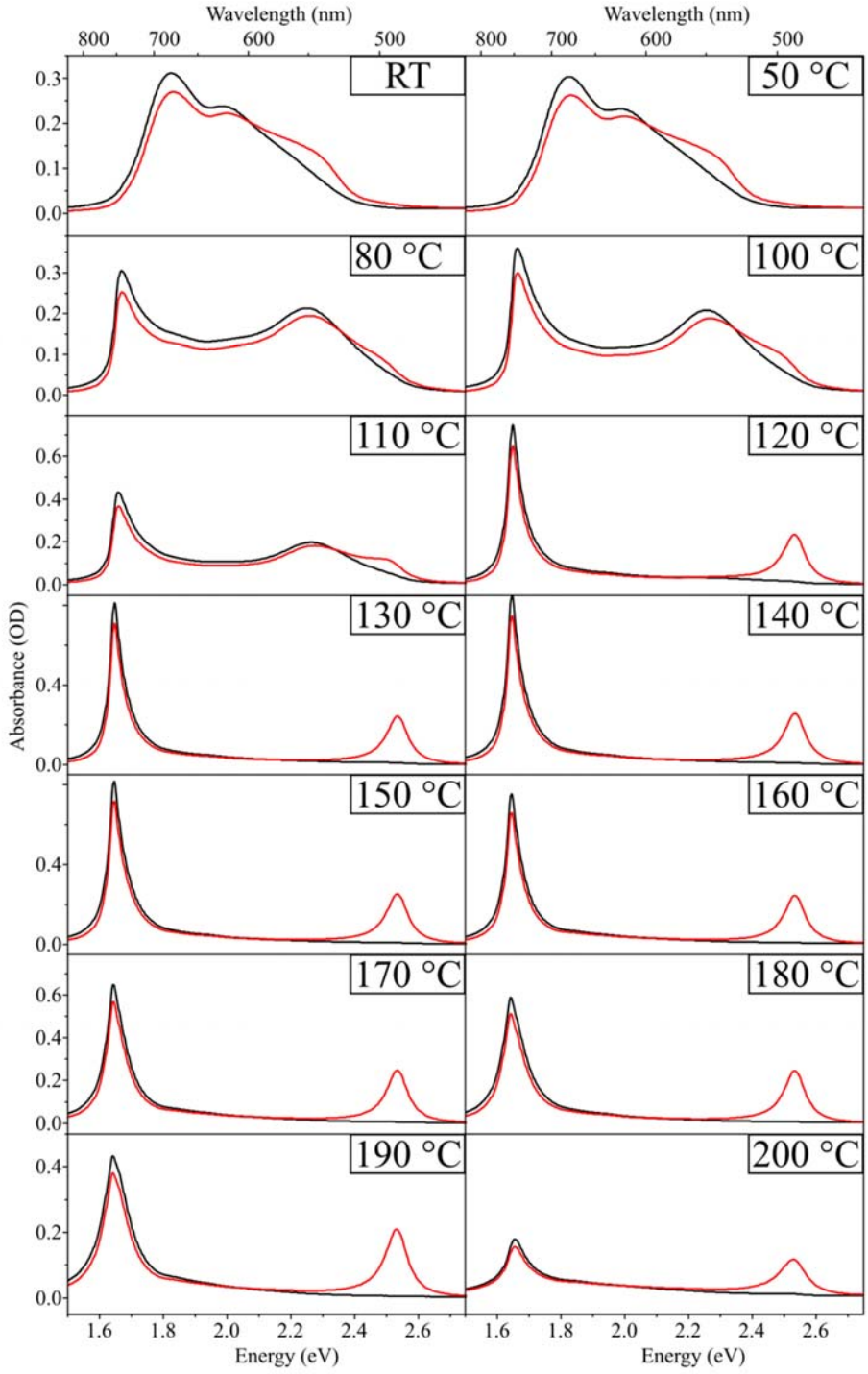

***Figure S17**: Absorption spectra of spin coated thin films on float glass at all investigated annealing temperatures, indicated in each panel, for normal incidence (black) and under 45° AOI for p-polarized light (red).*

Additionally to the extinction spectra on float glass substrates, the three different regimes observed in charge-carrier mobility measurements can clearly be distinguished by reflectivity measurements of the associated OFET-substrates too. Reflectivity measurements, shown in ***Figure S18***, were performed at an AOI of 50° for p-polarized light to observe both, the J- and H-transition spectral feature. In **regime I** no sharp spectral features are observed. However, a small peak around the H-transition energy (ca. 2.5 eV) is visible. Starting from annealing at 80 °C in **regime II** a sharp spectral feature around the J-transition energy (ca. 1.65 eV), typical for narrow and strong absorption, is measured and additionally the peak around the H-transition energy shows increasing intensity with increasing annealing temperature. Finally in **regime III** and at higher annealing temperatures both features, around the J- and H-transition energy exhibit sharp edges and dominate the spectra. At an annealing temperature of 200 °C the observed features are very weak due to desorption and melting of the material, however the J- and H-transition spectral features are still observed.

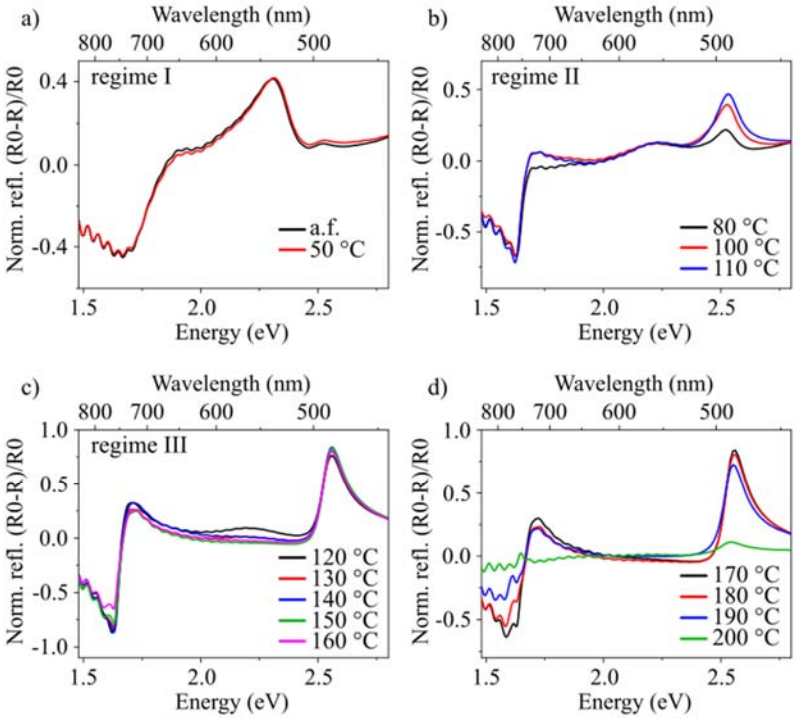

Figure S18*: Normalized reflectivity spectra of HB238 on OFET-substrates for different annealing temperatures, recorded at 50° AOI for p-polarized light. a) as fabricated and 50 °C (**regime I**), b) 80 °C – 110 °C (**regime II**), c) 120 °C – 160 °C (**regime III**), and d) 170 °C – 200 °C.*

In ***Figure S19***-**Figure S20** the output and transfer characteristics of the here investigated OFETs are presented for the different annealing temperatures. The output characteristics (top panels) of OFETs in **regimes I** and **II** do not show saturated drain currents and are thus only evaluated in the linear regime. In **regime III** the saturation of drain-current is clearly observed thus allowing the extraction of charge carrier mobility in the linear and saturation regime. The charge carrier

mobility was extracted according to Eqs. 1 and 2 in the main text by utilizing the linear fits, shown as red solid lines in the transfer characteristics (bottom panels).

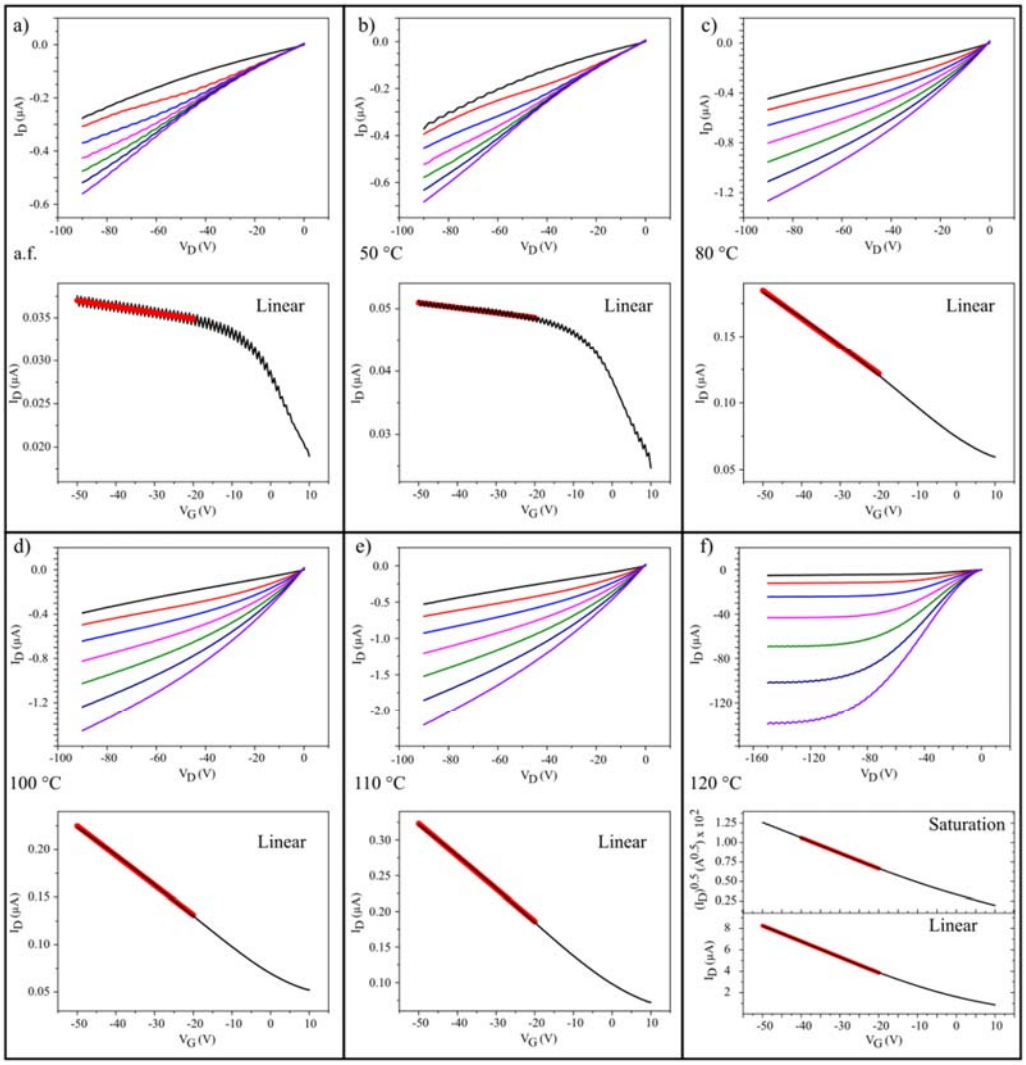

Figure S19*: Output (top) and transfer (bottom) characteristics of the a) non-annealed (a.f.) OFET and of OFETs annealed at b) 50 °C, c) 80 °C, d) 100 °C, e) 110 °C, and f) 120 °C. Output characteristics are plotted as drain-current as a function of drain-voltage for gate-voltages from +10 V to -50 V in 10 V steps. Transfer curves are plotted as drain-current and square root of drain-current as a function of gate-voltage in the linear and saturation regime, respectively. Linear fits to the transfer curves are shown in red.*

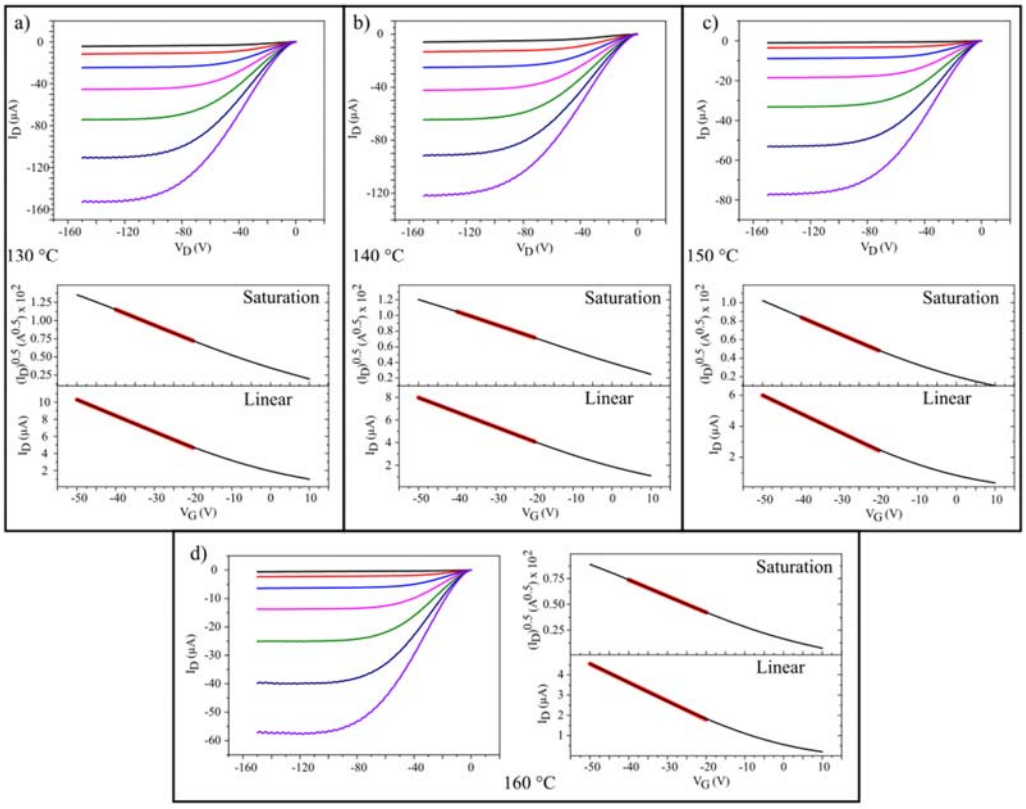

Figure S20*: Output (top) and transfer (bottom) characteristics of OFETs annealed at a) 130 °C, b) 140 °C, c) 150 °C, and d) 160 °C. Output characteristics are plotted as drain-current as a function of drain-voltage for gate-voltages from +10 V to -50 V in 10 V steps. Transfer curves are plotted as drain-current and square root of drain-current as a function of gate-voltage in the linear and saturation regime, respectively. Linear fits to the transfer curves are shown in red.*

Supporting Information part III: Estimation of coherence length

The theory as well as a detailed description about peak fitting is given in the main text in **Experimental techniques and methods**. **Figure S21** shows the absorption spectra of all spin coated thin films on float glass in **regimes II** and **III** measured at 45° AOI with p-polarized light, along with the corresponding fits of the J-, and H-transition absorption peaks respectively.

A few spectra were fitted exceptionally as explained in the following:

Fitting of the three spectra for films annealed at 80 °C, 100 °C, and 110 °C (see **Figure S21**) was done differently from the other spectra, whose treatment is given in the main text. Here, the high energy boundary for the J-transition extinction peak was chosen at the energy value which corresponds to approximately 80 % of the peak maximum, to minimize the influence of spectrally overlapping transitions even further. The associated H-transition absorption peak significantly overlaps with a broad transition at lower energies. To extract the H-transition peak parameters, both transitions were fitted with a cumulative fit of two asymmetric Voigt-profiles in an energy range between approximately 2.2 eV and 2.8 eV (see as well **Figure S21**).

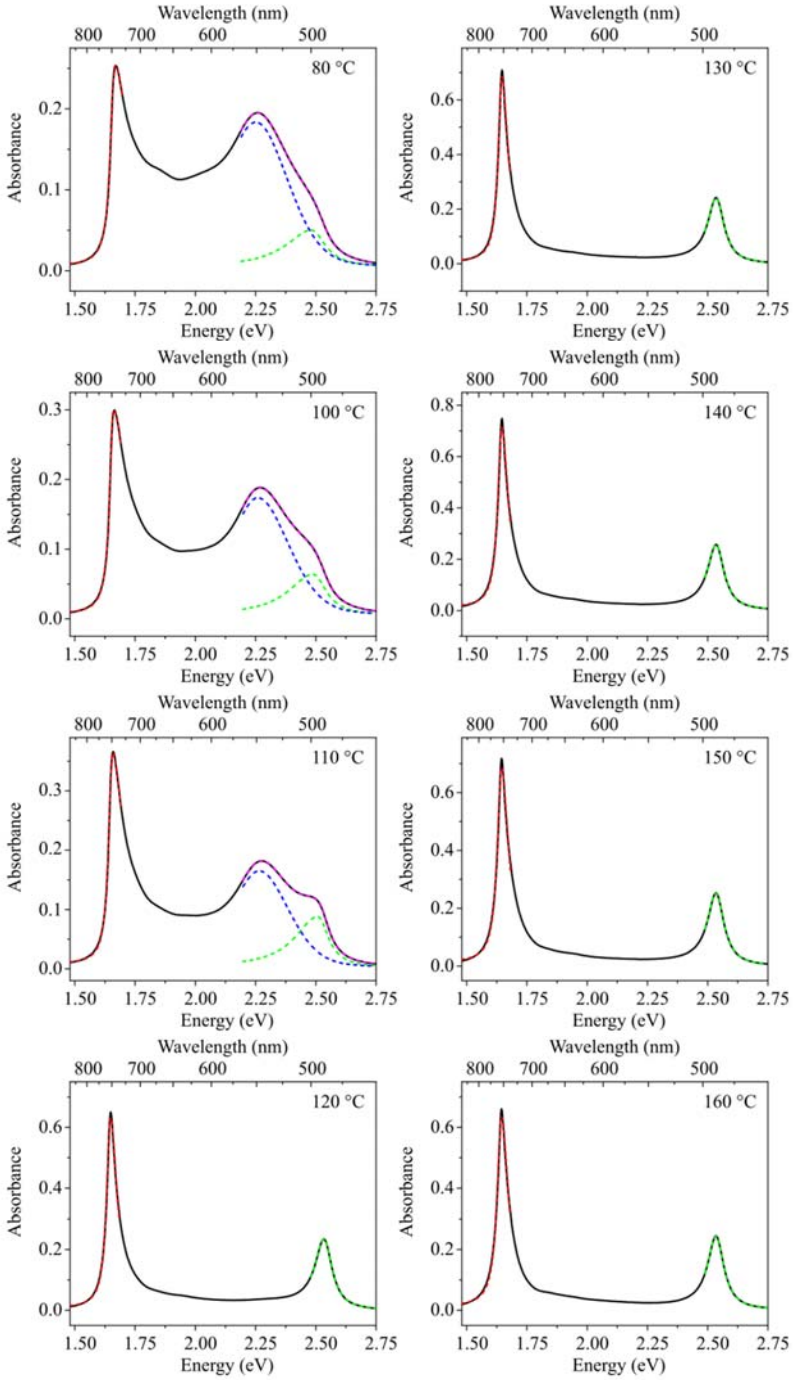

Figure S21*: Absorption spectra of spin coated thin films on float glass annealed at different temperatures between 80 °C and 160 °C (***regimes II** *and* **III***) recorded at 45° AOI for p-polarized light and corresponding fits for the J-transition (red dashed line) and H-transition (green dashed line). At annealing temperatures of 80 °C, 100 °C, and 110 °C (***regime II***) a cumulative fit (magenta dashed line) was used due to the spectral overlap of the H-transition and a broader red-shifted transition (blue dashed line). Details of the fitting procedure are described in* **methods** *in the main text.*

Supporting Information Part IV: Evaporated HB238 Thin Films on HOPG

Figure S22 shows reflectance spectra of a spincoated thin film on float glass (annealed at 120 °C) in comparison to reflectance spectra of thermally evaporated thin films on HOPG (80 °C substrate temperature) for different AOI for s- and p-polarized light.

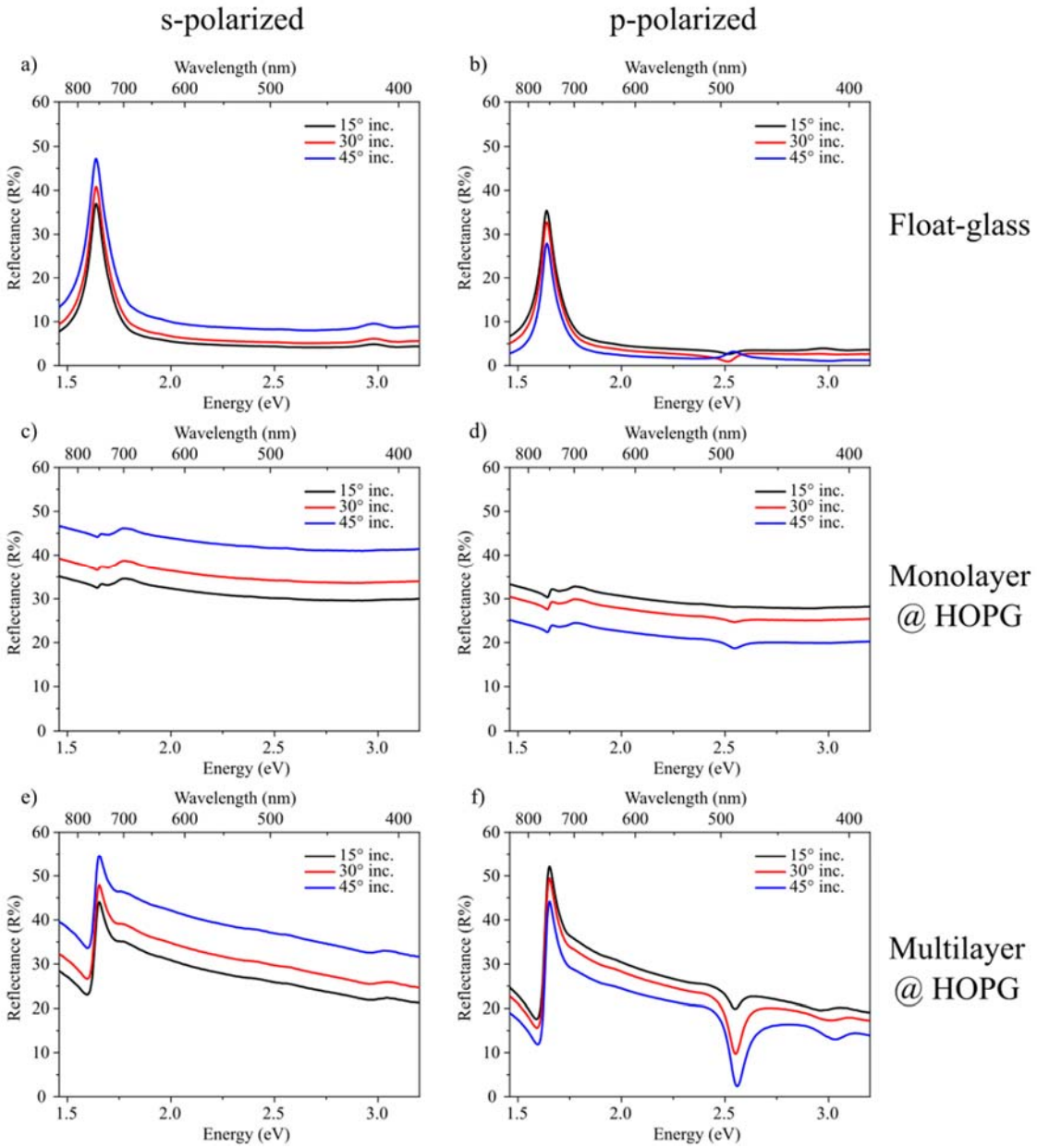

Figure S22*: Comparative reflectance spectra of HB238 thin films at different AOI for s- (left) and p-polarized (right) light. a) and b) Spin coated on float glass and annealed at 120 °C for 10 minutes. c) and d) Evaporated on HOPG (monolayer). e) and f) Evaporated on HOPG (multilayer).*

It is clearly observed that the spectral feature arising from the H-transition around 2.5 eV is only visible for p-polarized light (panels **b**, **d**, **f**), is more pronounced for increasing AOI, and is absent for s-polarized light (panels **a**, **c**, **e**) independent of the AOI. The J-transition spectral feature on the other hand is visible in all spectra. This applies to all thin films shown here, spin coated on float glass (annealed at 120 °C for 10 min.), and even more pronounced for thermally evaporated thin films on HOPG. This confirms that the investigated thin films on HOPG too exhibit uniaxial anisotropy, with an out-of-plane H-transition and an in-plane J-transition.

Figure S23 shows AFM images of the mono- (panel **a**) and multilayer (panel **b**) on HOPG, along with extracted linear height profiles on the observed elevated (face-on) crystallites. The measured step-size on those crystallites is around 0.5 nm. According to the approximate molecular dimensions (panel **b**) the only possible molecular orientation reflecting the measured step heights is a face-on orientation, denoting that the molecules pack with their conjugated π-systems parallel to the HOPG surface-plane. Panels **c** and **d** show the spatially correlated PL micrographs for vertical excitation polarization and representative normalized PL-spectra measured at positions indicated by white and black circles in the PL micrographs measured with vertical excitation and emission polarization. Contrary to the edge-on structure, the dependence on linear excitation and emission polarization of the face-on crystallites is not trivial and is not further discussed here. However, the spectral shape is similar between all possible combinations of vertically and horizontally polarized excitation and emission. PL-spectra are shown for edge-on structures and face-on crystallites for comparison. The face-on crystallite emission maximum is blue-shifted relative to the edge-on structure emission by approximately 50 meV. It is further composed of at least two spectrally close emission peaks and differs in spectral shape between different face-on crystallites. Additionally, a broad spectral feature is observed around 1.6 eV, whose origin is undefined, but could result from trap-states, uncoupled monomers, or dimers, typical for broad spectral emission.[S14] Compared with the monomer emission (see **Figure 1b** in main text) the face-on crystallites emission is as well red-shifted, hinting for some kind of J-transition emission.

The summarized results of AFM, PL-microspectroscopy, absorption spectroscopy, and XRD investigations are presented in **Figure S24**. The morphology measured with AFM is shown in panel a). Grains of a size of ca. 3µm in diameter maximum are observed, which are separated by pronounced grain boundaries, and exhibit random in-plane orientation. The elevated structure visible at the top right of the image stems from a scratch, intentionally inflicted on the sample, to find the same sample position for the PL-study. The correlated PL micrograph are shown in panel b). The polarization of the excitation beam has a strong influence on the emission intensity of each HB238 crystal grain. Moreover, in combination with the AFM topography shown in **Figure S24** the random orientation of the grains relative to each other is clearly visible. We confirm the presence of the same edge-on aggregate species in the evaporated thin film on float glass, as found for all other sample types in this work, by PL- and absorption spectroscopy as well as XRD measurements. The results are shown in **Figure S24c-e** and can be compared with e.g. ***Figure S12-Figure S14*** (PL), ***Figure S17*** (Anisotropic Abs.), or ***Figure S3*** (XRD).

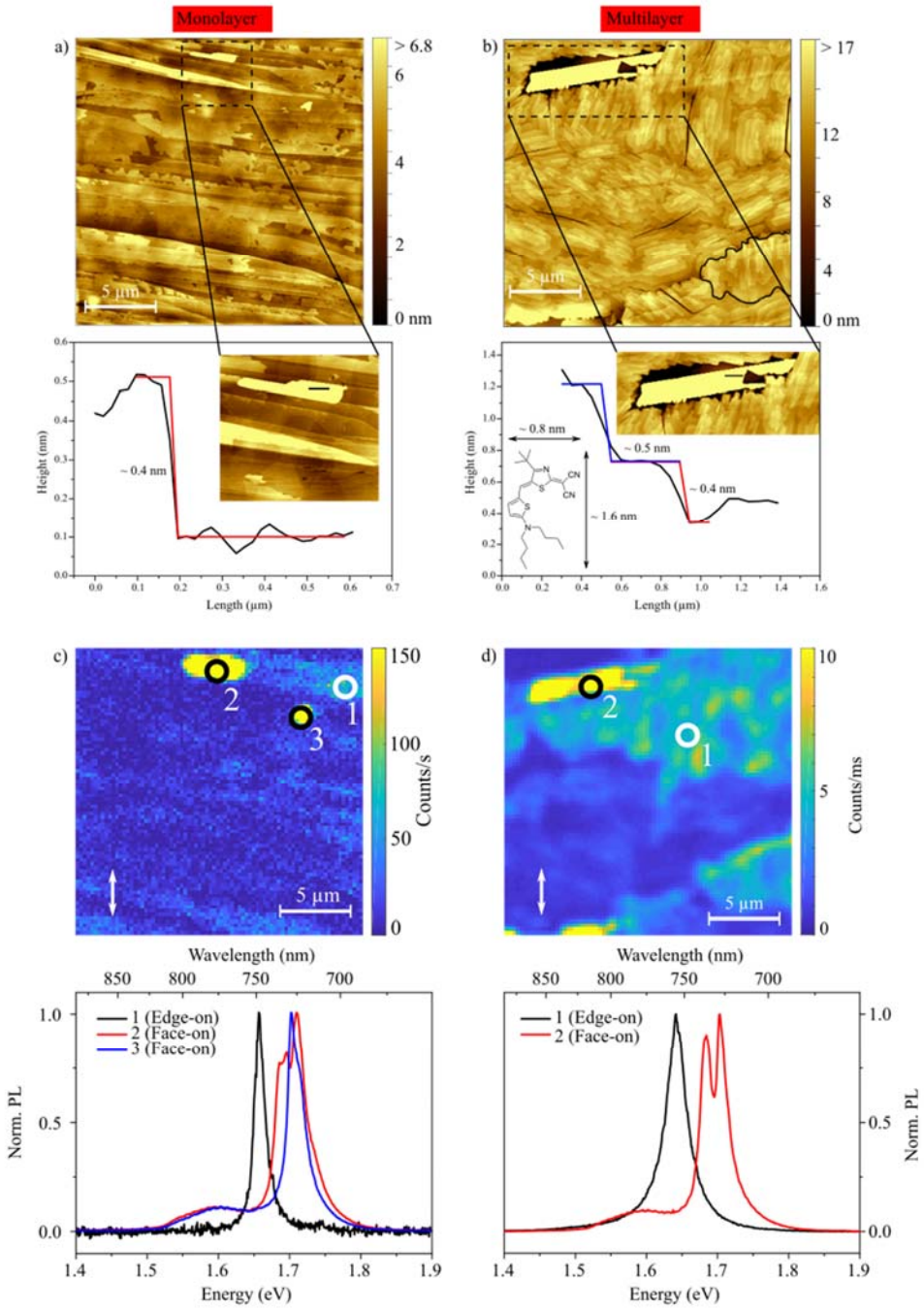

Figure S23: *Comparative AFM and PL-microspectroscopy on HB238 face-on crystallites on evaporated mono- (left) and multilayer (right) on HOPG. a) and b) AFM images along with linear height profiles extracted on the face-on crystallite's surface. The approximate molecular dimensions are shown as well in panel* **b**, *indicative for the face-on molecular arrangement in the investigated crystallites. c) and d) PL micrographs along with normalized PL-spectra recorded at positions indicated with white and black circles. For comparison spectra are shown for both, edge-on and face-on structures.*

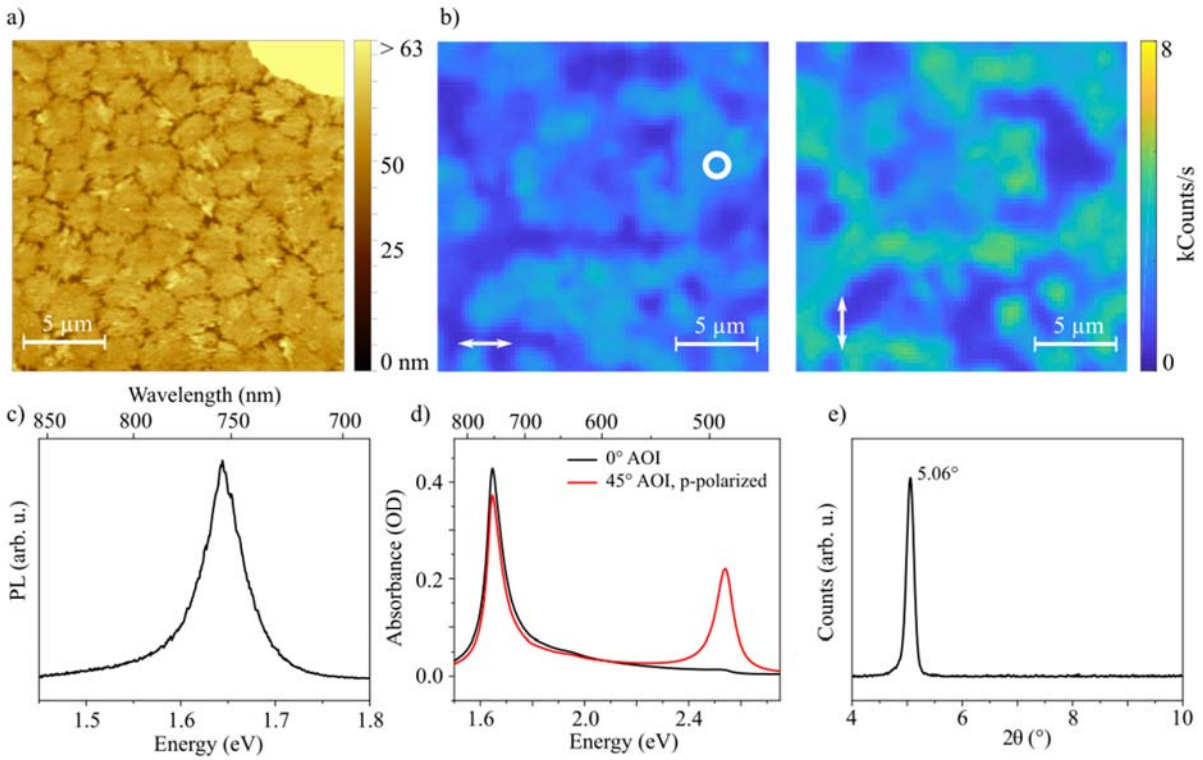

Figure S24: *Summarized results of an evaporated HB238 multilayer on float glass. a) AFM topography 20 µm by 20 µm area. b) PL micrographs at the same sample area as in a) for horizontally (left) and vertically (right) polarized excitation. The white circle indicates at which position the PL-spectrum shown in c) was recorded. c) PL-spectrum measured at the position indicated by the white circle in panel b). d) Absorption spectrum measured at normal incidence (black) and at an AOI of 45° for p-polarized light (red). e) 2θ-XRD pattern.*

References Supporting Information

(S1) Bürckstümmer, H.; Tulyakova, E. V; Deppisch, M.; Lenze, M. R.; Kronenberg, N. M.; Gsänger, M.; Stolte, M.; Meerholz, K.; Würthner, F. Efficient Solution-Processed Bulk Heterojunction Solar Cells by Antiparallel Supramolecular Arrangement of Dipolar Donor–Acceptor Dyes. *Angew. Chemie Int. Ed.* **2011**, *50*, 11628–11632.

(S2) Bakalis, L. D.; Knoester, J. Linear Absorption as a Tool to Measure the Exciton Delocalization Length in Molecular Assemblies. *J. Lumin.* **2000**, *87*, 66–70.

(S3) Xu, Y.; Li, Y.; Li, S.; Balestra, F.; Ghibaudo, G.; Li, W.; Lin, Y. F.; Sun, H.; Wan, J.; Wang, X.; Guo, Y.; Shi, Y.; Noh, Y. Y. Precise Extraction of Charge Carrier Mobility for Organic Transistors. *Adv. Funct. Mater.* **2019**, *1904508*, 1–23.

(S4) Spek, A. L. PLATON SQUEEZE: A Tool for the Calculation of the Disordered Solvent Contribution to the Calculated Structure Factors. *Acta Crystallogr. Sect. C Struct. Chem.* **2015**, *C71*, 9–18.

(S5) Sheldrick, G. M. SHELXT - Integrated Space-Group and Crystal-Structure Determination. *Acta Crystallogr. Sect. A Found. Crystallogr.* **2015**, *A71*, 3–8.

(S6) Sheldrick, G. M. Crystal Structure Refinement with SHELXL. *Acta Crystallogr. Sect. C Struct. Chem.* **2015**, *C71*, 3–8.

(S7) Frisch, M. J.; Trucks, G. W.; Schlegel, H. B.; Scuseria, G. E.; Robb, M. A.; Cheeseman, J. R.; Scalmani, G.; Barone, V.; Petersson, G. A.; Nakatsuji, H.; Li, X.; Caricato, M.; Marenich, A. V.; Bloino, J.; Janesko, B. G.; Gomperts, R.; Mennucci, B.; Hratchian, H. P.; Ortiz, J. V.; Izmaylov, A. F.; Sonnenberg, J. L.; Williams-Young, D.; Ding, F.; Lipparini, F.; Egidi, F.; Goings, J.; Peng, B.; Petrone, A.; Henderson, T.; Ranasinghe, D.; Zakrzewski, V. G.; Gao, J.; Rega, N.; Zheng, G.; Liang, W.; Hada, M.; Ehara, M.; Toyota, K.; Fukuda, R.; Hasegawa, J.; Ishida, M.; Nakajima, T.; Honda, Y.; Kitao, O.; Nakai, H.; Vreven, T.; Throssell, K.; Montgomery Jr., J. A.; Peralta, J. E.; Ogliaro, F.; Bearpark, M. J.; Heyd, J. J.; Brothers, E. N.; Kudin, K. N.; Staroverov, V. N.; Keith, T. A.; Kobayashi, R.; Normand, J.; Raghavachari, K.; Rendell, A. P.; Burant, J. C.; Iyengar, S. S.; Tomasi, J.; Cossi, M.; Millam, J. M.; Klene, M.; Adamo, C.; Cammi, R.; Ochterski, J. W.; Martin, R. L.; Morokuma, K.; Farkas, O.; Foresman, J. B.; Fox, D. J. *Gaussian 16*; Revision B.01.; Gaussian, Inc.: Wallingford CT, 2016.

(S8) Giannozzi, P.; Baroni, S.; Bonini, N.; Calandra, M.; Car, R.; Cavazzoni, C.; Ceresoli, D.; Chiarotti, G. L.; Cococcioni, M.; Dabo, I.; Dal Corso, A.; De Gironcoli, S.; Fabris, S.; Fratesi, G.; Gebauer, R.; Gerstmann, U.; Gougoussis, C.; Kokalj, A.; Lazzeri, M.; Martin-Samos, L.; Marzari, N.; Mauri, F.; Mazzarello, R.; Paolini, S.; Pasquarello, A.; Paulatto, L.; Sbraccia, C.; Scandolo, S.; Sclauzero, G.; Seitsonen, A. P.; Smogunov, A.; Umari, P.; Wentzcovitch, R. M. QUANTUM ESPRESSO: A Modular and Open-Source Software Project for Quantum Simulations of Materials. *J. Phys. Condens. Matter* **2009**, *21*, 395502.

(S9) Ge, X.; Binnie, S. J.; Rocca, D.; Gebauer, R.; Baroni, S. TurboTDDFT 2.0 - Hybrid Functionals and New Algorithms within Time-Dependent Density-Functional Perturbation Theory. *Comput. Phys. Commun.* **2014**, *185*, 2080–2089.

(S10) Heinemeyer, U.; Scholz, R.; Gisslén, L.; Alonso, M. I.; Ossó, J. O.; Garriga, M.; Hinderhofer, A.; Kytka, M.; Kowarik, S.; Gerlach, A.; Schreiber, F. Exciton-Phonon Coupling in Diindenoperylene Thin Films. *Phys. Rev. B - Condens. Matter Mater. Phys.* **2008**, *78*, 085210.

(S11) Gildemeister, N.; Ricci, G.; Böhner, L.; Neudörfl, J. M.; Hertel, D.; Würthner, F.; Negri, F.; Meerholz, K.; Fazzi, D. Understanding the Structural and Charge Transport Property Relationships for a Variety of Merocyanine Single-Crystals: A Bottom up Computational Investigation. *J. Mater. Chem. C* **2021**.

(S12) Spek, A. L. PLATON SQUEEZE: A Tool for the Calculation of the Disordered Solvent Contribution to the Calculated Structure Factors. *Acta Crystallogr. Sect. C Struct. Chem.* **2015**, *C71*, 9–18.

(S13) Triscone, J.-M.; Fivat, P.; Andersson, M.; Decroux, M.; Fischer, Ø. Two-Dimensional and Three-Dimensional Vortex Lattice Dynamics in DyBa2Cu3O7-(Y1-XPrx)Ba2Cu3O7 Coupled Heterostructures. *Phys. Rev. B* **1994**, *50*, 1229–1236.

(S14) Sorokin, A. V.; Pereverzev, N. V.; Grankina, I. I.; Yefimova, S. L.; Malyukin, Y. V. Evidence of Exciton Self-Trapping in Pseudoisocyanine J-Aggregates Formed in Layered Polymer Films. *J. Phys. Chem. C* **2015**, *119*, 27865–27873.

(S15) Liess, A.; Lv, A.; Arjona-Esteban, A.; Bialas, D.; Krause, A.-M.; Stepanenko, V.; Stolte, M.; W⎫rthner, F.; *Nano Lett*. **2017**, *17*, 1719-1726